

# Deeply Virtual Compton Scattering off $^4\text{He}$

K. Hafidi<sup>†\*</sup>, J. Arrington, L. El Fassi, D.F. Geesaman, R. J. Holt,  
B. Mustapha, D. H. Potterveld, P. E. Reimer, P. Solvignon

*Argonne National Laboratory, Argonne IL 60439, USA*

F.-X. Girod<sup>†</sup>, H. Avakian, V. Burkert, A. Camsonne,  
L. Elouadrhiri, H. Fenker, V. Kubarovsky, V. Guzey, S. Stepanyan

*Jefferson Laboratory, Newport News, VA 23606, USA*

E. Voutier<sup>†</sup>, J. Ball, P.-Y. Bertin<sup>1</sup>, A. El Alaoui, A. Fradi,  
E. Fuchey, M. Garçon, M. Guidal, C.E. Hyde<sup>2</sup>, F. Itard,  
P. Konczykowski, M. Mac Cormick, B. Michel, B. Moreno,  
C. Muñoz Camacho, S. Niccolai, B. Pire, S. Procureur, F. Sabatié,  
S. Wallon

*CPhT Ecole Polytechnique (Palaiseau) / IPN (Orsay) / LPC (Clermont-Ferrand)  
LPSC (Grenoble) / LPT (Orsay) / SPhN (Saclay)  
CEA/DSM/DAPNIA & CNRS/IN2P3, France*

M. Amarian, S. Bueltmann, G. Gavalian, S. Kuhn

*Old Dominion University, Norfolk, VA 23529, USA*

H. Egiyan<sup>†</sup>, J. Calarco, M. Holtrop, L. Zana

*University of New Hampshire, Durham, NH 03824, USA*

S. Liuti<sup>†</sup>, S. Ahmad

*University of Virginia, Charlottesville, VA 22904-4714, USA*

M. Mazouz

*Faculté des Sciences de Monastir, 5000 Monastir, Tunisia*

W. Brooks

*Universidad Técnica Federico Santa María, Valparaíso, Chile*

F. Benmokhtar

*Carnegie Mellon University, Pittsburg, PA 15213, USA*

P. Cole, D. Dale, T. Forest

*Idaho State University, Pocatello, ID 83201, USA*

## A CLAS Collaboration proposal

† Co-spokesperson

\* Contact: Kawtar Hafidi (kawtar@anl.gov)

---

<sup>1</sup> and Jefferson Laboratory, Newport News, VA-23606, USA

<sup>2</sup> and Old Dominion University, Norfolk, VA 23529, USA

---

**Abstract**

We propose to measure the Beam Spin Asymmetry (BSA) in Deeply Virtual Compton Scattering (DVCS) off  $^4\text{He}$ . The measurements will use a 6 GeV polarized electron beam, a  $^4\text{He}$  pressurized gas target, the CLAS and the BoNuS RTPC detectors. The major goal of this proposal is to perform the first fully quantitative investigation of the DVCS reaction off a nuclear target in the coherent and incoherent channels. The spin zero of the  $^4\text{He}$  target allows for a simple parametrization of its partonic structure characterized at leading twist by one chirally-even Generalized Parton Distribution  $H_A$ . This experiment proposes a model-independent extraction of the real and imaginary parts of the Compton form factor  $\mathcal{H}_A(x_B, t)$  from the BSA measured in the  $^4\text{He}(\vec{e}, e'\gamma^4\text{He})$  coherent channel. The  $x_B$  and  $t$  evolution of these quantities will be studied, allowing us to explore the spatial distribution of the strong interactions between partons in a nucleus. The BSA of the  $^4\text{He}(\vec{e}, e'\gamma p)$  incoherent channel will be simultaneously measured. The comparison of both measurements with the CLAS free proton data will allow us to address novel nuclear effects such as the role of the transverse degrees of freedom in the nuclear structure and to study their contributions to the EMC effect. This proposal requests 45 days of highly polarized electron beam that can run concurrently with the approved experiment E07-009.

---

## Contents

1	Introduction	6
2	Physics Motivations	8
3	Experimental Observables	12
3.1	Deeply Virtual Compton Scattering	12
3.2	Beam Spin Asymmetry	13
4	Experimental Overview	15
5	Experimental Setup	16
5.1	CLAS Setup	17
5.2	BoNuS RTPC	18
5.3	Internal Calorimeter	19
5.4	Beamline	21
5.5	Trigger	22
6	Measurements	22
6.1	Kinematic Coverage	23
6.2	Exclusivity	26
6.3	Background Subtraction	28
6.4	Extraction of Asymmetries	30
7	Beam Time Request	30
7.1	Projections	30
7.2	Extraction of $\mathcal{H}_A$ Compton form factor	34
7.3	Systematic uncertainties	35
7.4	Beam Time Request	36
8	Relation to Other Experiments	37
9	Summary	37

10	Appendix A	38
10.1	Bethe-Heitler propagators	38
10.2	Fourier coefficients of a spin-0 target	38
10.3	Fourier coefficients of spin-1/2 target	39
11	Appendix B	42
11.1	Upgrade of the RTPC readout hardware	42
	References	44

# 1 Introduction

The observation by the European Muon Collaboration (EMC) of a deviation of the deep inelastic structure function of a nucleus from the sum of the structure functions of the free nucleons, the so-called EMC effect [1], showed that the nuclear environment has a significant impact on hard hadronic processes [2,3]. Theoretical and experimental efforts throughout the years have led to the identification of four kinematical regions where different types of deviations can be observed and different effects might be at play: the shadowing region ( $0.1 < x_B$ ), the anti-shadowing region ( $0.1 < x_B < 0.2$ ), the "EMC-effect" region ( $0.2 < x_B < 0.7$ ) and the  $x_B > 0.7$  region where Fermi motion of the nucleons is expected to play a major role (see Fig. 1). Physical interpretations in most of the kinematical range remain quite elusive, with the exception perhaps of the shadowing and very large  $x_B$  regions where coherent effects and Fermi motion effects are at play, respectively.

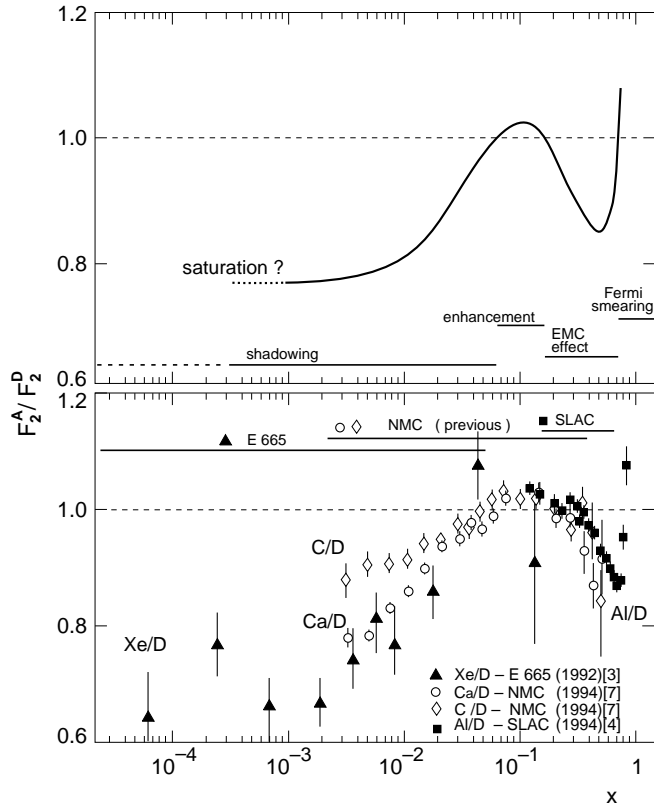


Fig. 1. Sketch of the EMC effect as seen from the ratio of the nuclear to deuteron structure functions per nucleon (upper panel); measurements of the EMC effect in C, Ca, Al and Xe [4] (lower panel).

From various experimental observations in nuclear deep inelastic scattering (DIS) and related processes, it becomes clear that even in a DIS process characterized by high locality of the probe-target interaction region, a different picture emerges from the nucleus other than a collection of quasi-free nu-

cleons. The bound nucleon properties and interactions appear instead to be modified in different ways ranging from *e.g.* nuclear dependent changes of the color string tension, or of the confinement scale in cold nuclear matter, therefore bearing important consequences on our understanding of the origin of hadronic mass. A unifying physical picture is still a matter of intense debate. Throughout the years theoretical efforts have however reached a higher level of sophistication including: new applications of effective theories [5–7], the role of transverse degrees of freedom and partonic reinteractions [8], the role of diquarks in the nuclear medium [9] and its connection to color-superconducting quark matter [10,11], and elaborate studies of the impact of the modifications of the confinement scale [12] or of the string tension for bound nucleons [13]. Hard exclusive experiments such as Deep Virtual Compton Scattering (DVCS) and Deep Virtual Meson Production (DVMP) provide an important new probe that will allow us to discern among different interpretations by introducing a new framework to describe both the intrinsic motion of partons and their transverse spatial structure in nuclei [8,14]. Valuable information can be obtained from the measurement of the nuclear Generalized Parton Distributions (GPDs) representing the soft matrix elements for these processes.

The aim of this proposal is to perform a first, fully quantitative investigation of DVCS off a nuclear target. DVCS has emerged as a powerful tool to investigate the quark and gluon structure of hadronic matter [15,16]. Similarly to the elastic scattering of light by a crystal, the scattering of energetic photons off the nucleus in the Bjorken regime tells us about the momentum and position distributions of the quarks and the gluons. These features are described within the recent GPDs formalism [17] which provides a comprehensive picture of the structure of hadrons. GPDs correspond to the coherence between quantum states of different (or same) helicity, longitudinal momentum, and transverse position. In an impact parameter space they can be interpreted as a distribution in the transverse plane of partons carrying a certain longitudinal momentum [18–20]. A crucial feature of GPDs is the access to the transverse position of partons which, combined with their longitudinal momentum, leads to the total angular momentum of partons [21]. This information is inaccessible to inclusive deep inelastic scattering (DIS) which measures probability amplitudes in the longitudinal plane.

Recent experiments at the Jefferson Laboratory (JLab) [22,23] are consistent with the dominance of the handbag diagram in the description of the DVCS process on the nucleon. It is the goal of this proposal to employ the DVCS reaction in the coherent and incoherent channels for the investigation of the internal structure of the  $^4\text{He}$  nucleus. These measurements will provide new insight on the partonic structure of the nucleus and will allow us to address novel nuclear effects such as the role of transverse degrees of freedom or the spatial distribution of the strong interactions among partons in nuclei. The comparison between the coherent and the incoherent channels will allow us to

access different information on the parton distributions in transverse space: coherent scattering will provide a measurement of the impact parameter dependent parton distributions inside the nucleus, while incoherent scattering will isolate specifically partonic configurations of the bound nucleons.

## 2 Physics Motivations

The formulation of hard exclusive processes in terms of GPDs [17,24,25] has transformed both the experimental and theoretical approaches for probing deep inelastic hadronic structure. GPDs provide a framework to describe in a partonic language the orbital angular momentum carried by the nucleon's constituents [24]. In addition, they give the unprecedented possibility to access the spatial distributions of quarks and gluons. As shown in Refs. [18,19,26], the perpendicular component of the momentum transfer  $t$  entering the GPDs is the Fourier conjugate of the transverse distance of the partons in the infinite momentum frame.

The exciting possibility of mapping out the transverse spatial structure of hadrons stimulated a series of DVCS experiments [22,23,27–33]. Measurements at Jefferson Lab have been particularly successful in showing the scaling behavior of the cross section [22,23]; they have lead the way of the extraction of unpolarized GPDs for both the proton [22] and neutron [33] in a given kinematical range of  $t$ . In addition, the accuracy reached in recent DVCS experiments at Jefferson Lab concretely opens the new prospect of exploring partonic spatial distributions also in nuclei. This is definitely a most desirable perspective. In fact, from the inception of the EMC effect it becomes clear that spatial components such as confinement sizes, as well as overlap and deconfinement probabilities, play a most important role in nuclei. Configuration size modifications have been advocated as responsible for the behavior of the EMC ratio in the intermediate  $x_B$  region. The generalized EMC effect *i.e.* the modification of the nuclear GPDs with respect to the free nucleon ones, normalized to their respective form factors was studied in Refs. [8,34–36].

Due to its spin-0 and high density, the  ${}^4\text{He}$  nucleus constitutes an ideal target for disentangling those nuclear effects that can be related to the forward unpolarized EMC effect [1]. Studies of nuclei with different spin, such as the deuteron, involve completely new functions with respect to the forward case therefore making these investigations more difficult. Measurements in the range  $0.1 \lesssim x_B \lesssim 0.6$ , and for an appropriate  $t$ -range are crucial for both establishing the role of partonic configurations sizes in nuclei, and for discerning among the several competing explanations of the EMC effect. As shown in Ref. [8], the role of partonic transverse degrees of freedom, both in momentum and coordinate space, is enhanced in the generalized EMC effect, thus predict-

ing an enhancement of signals of nuclear effects with respect to the forward case (Fig. 2).

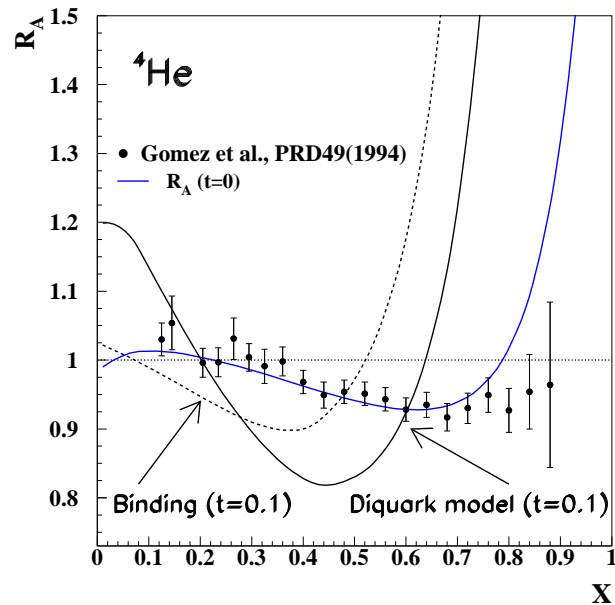


Fig. 2. Off-forward EMC effect in  ${}^4\text{He}$ . Theoretical predictions at  $t = 0.1 \text{ GeV}^2$  from both “conventional” binding models and within a diquark picture for nuclear modifications are shown. For comparison we show the effect at  $t = 0$  along with the experimental data [37] (adapted from Ref. [38]).

In addition, a number of interesting relationships were found by studying Mellin moments in nuclei: the  $A$ -dependence for the  $D$ -term of GPDs was estimated within microscopic approaches [8,35], and compared with the calculation of Ref. [39] using a liquid drop model; a connection was made in Ref. [8] with the widely used approaches that relate the modifications of “partonic” parameters such as the string tension, or the confinement radius, to density dependent effects in the nuclear medium (see Ref. [13] and references therein).

All of the above theoretical ideas and experimental results designate nuclear GPDs as a potentially important new tool to investigate in-medium modification effects and related phenomena, which are vital for interpreting both current and future data on hard processes in nuclei.

For a nuclear target there exist two distinct processes:

- (1) the scattering proceeds coherently, i.e. the target nucleus recoils as a whole while emitting a photon with momentum  $q'$  (Fig. 3a);
- (2) the scattering proceeds incoherently, i.e. the nucleus undergoes a breakup and the final photon is emitted from a quasi-elastically scattered nucleon (Fig. 3b).

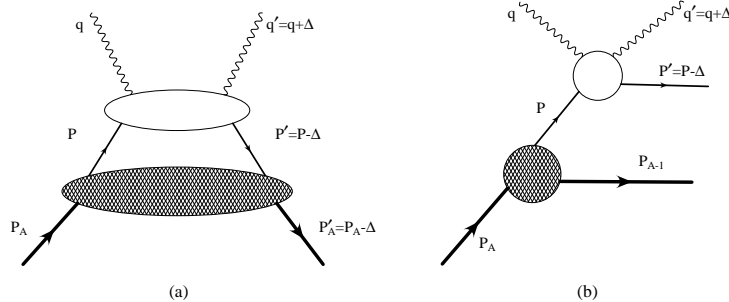


Fig. 3. DVCS processes from a nuclear target at leading order in  $Q$ : **(a)** coherent process; **(b)** incoherent process.

The relative contributions of these two processes in  ${}^4\text{He}$  were calculated by Liuti and Taneja [8] and by Guzey and Strikman [34]. Guzey and Strikman consider that the nucleus to proton beam spin asymmetries ratio  $A_{LU}^{4\text{He}}/A_{LU}^p$  for the coherent process is enhanced with respect to the proton case due to the presence of an  $A$ -dependent combinatorial factor counting the number of ways the final photon can be emitted by different nucleons. On the contrary, the same ratio in the incoherent case is estimated to be equal to one, disregarding nuclear binding effects. Therefore, when the coherent and incoherent processes are not separated a steep  $t$ -dependence for small  $t$  ( $t < 0.06 \text{ GeV}^2$  in Ne and Kr) arises followed by a flat behavior as the asymmetry ratio becomes dominated by incoherent scattering and it approaches unity [34]. Liuti and Taneja [8] propose instead a dynamical mechanism.  $A$ -dependent effects are predicted to appear for both the coherent and incoherent cases because of the presence of a generalized EMC effect *i.e.* a modification of the nuclear GPDs with respect to the free nucleon ones. Most importantly, the presence of partonic transverse degrees of freedom, which are accounted for in a quark-diquark model for bound hadronic configurations in the nucleus, appears to produce an enhanced generalized EMC effect, with respect to the DIS case ( $t = 0 \text{ GeV}^2$ ). In this model both coherent and incoherent contributions are predicted to have similar magnitudes. The difference between the coherent and incoherent processes is given by the fact that in coherent scattering both the GPDs of the bound “package” (nucleon, three quark bag,  $\Delta$ , etc..) and the light cone distribution of nucleons inside the nucleus are off-forward quantities *i.e.*  $t$ -dependent observables (Fig. 3a). In incoherent scattering one has instead that: *i)* a bound nucleon is clearly distinguished from other possible nuclear constituents/packages containing the active quark; *ii)* the process involves the GPDs of the bound nucleon, similarly to the coherent case, but the light cone distribution for the nucleons is forward, *i.e.* evaluated at  $t = 0 \text{ GeV}^2$ .

It is interesting to notice that by Fourier transforming the nuclear GPD  $H_A$  extracted from the experiment in a model independent way, one can eventually access the impact parameter  $b$  dependent parton distributions,  $q_A(x_B, b)$  [40,41] in a nuclear environment. In a nucleus, three types of transverse coordinates can in fact be defined: the transverse separation between quarks in a

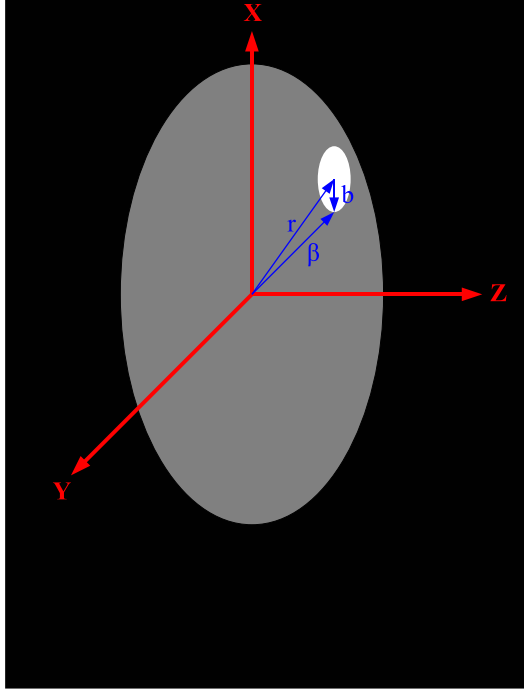


Fig. 4. Spatial coordinates of the quarks in a nucleus.

bound nucleon/nuclear constituent  $b$ , the transverse separation between nucleons  $r$ , and the transverse separation between quarks in the nucleus  $\beta$  (Fig. 4). This attractive possibility pointed out in Ref. [42], would enable to obtain quantitative information on *e.g.* the confinement size of bound nucleons, as well as on the transverse overlap areas of hadronic configurations inside the nucleus.

The proposed experiment offers to measure coherent DVCS Beam Spin Asymmetries (BSA) in order to extract for the first time and in a model independent way both the real and imaginary part of the  $^4\text{He}$  nuclear Compton form-factors  $\mathcal{H}_A(x_B, t)$ . Although this extraction covers a limited kinematical range ( $0.1 < x_B < 0.35$  and  $0.1 \text{ GeV}^2 < t < 0.22 \text{ GeV}^2$ ), it will lead the way toward the determination of the nucleus 3D picture in terms of its fundamental degrees of freedom. The comparison between the coherent BSA and the Hall B measurements on the proton will allow us to study the anti-shadowing region where the convolution model [8] predicts a 10 % enhancement compared to the nuclear inclusive DIS measurements. The same model predicts both a shift of the EMC effect dip from  $x_B = 0.6$  to  $x_B = 0.4$  and a 20 % enhancement of the signal. Complementary to the coherent measurements, the incoherent ones will allow to reach higher  $t$  values up to 0.35 and higher  $x_B$  regime up to 0.45 with good statistics where the same model predicts  $\sim 30$  % effect for the asymmetry ratio in the EMC region and  $\sim 15$  % in the anti-shadowing regime.

In summary, the proposed measurements will explore both the anti-shadowing and EMC regimes which are ideal for testing the differences among theoretical

models. The extraction of both the coherent and incoherent channels provides important new information that will help unravel the origin of the forward EMC effect. In the case of incoherent scattering the package is clearly identified with a nucleon, and no information on its transverse position can be obtained, at variance with the coherent case. Nevertheless, even in this case important information on bound nucleons deformations can be obtained. In coherent scattering other configurations are in principle allowed to contribute, and their position will be displaced from the center of the nucleus. It will be therefore of great physical significance to be able to compare results from both coherent and incoherent scattering.

### 3 Experimental Observables

#### 3.1 Deeply Virtual Compton Scattering

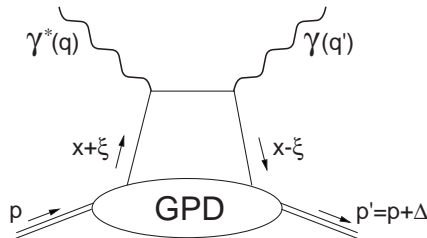


Fig. 5. Lowest order (QCD) amplitude for the virtual Compton process, the so-called handbag diagram.  $q, q'$  represent the the four-momentum of the virtual and real photons, and  $p, p'$  are the initial and final four-momentum of the target nucleus.

GPDs are universal non-perturbative objects, entering the description of hard exclusive electroproduction processes. They are defined for each quark flavor  $f$  and gluon as matrix elements of lightcone operators [16] describing the transition between the initial and final states of a hadron. The GPDs depend on two longitudinal momentum fraction variables ( $x, \xi$ ) and on the momentum transfer  $t$  to the target.  $x$  is the average longitudinal momentum fraction of the parton involved in the process and  $\xi$  is the longitudinal fraction of the momentum transfer  $\Delta$ , with  $\Delta^2 = t = (p - p')^2$  (Fig. 5). Particularly, its perpendicular component  $\Delta_{\perp}$  is Fourier conjugate to the transverse position of the parton in the impact parameter space. The spin zero of the  ${}^4\text{He}$  target allows for a simple parametrization of its partonic structure characterized at leading twist by one chirally-even GPD  $H_A$ . In the forward limit ( $t \rightarrow 0$ ), this GPD reduces to the usual parton densities of  ${}^4\text{He}$  measured in DIS. The polynomiality property of GPDs leads to interesting consequences: the first Mellin moment provides an explicit link with the electromagnetic form factor

$F_A$  of the nucleus

$$\sum_f e_f \int_{-1}^1 dx H_A^f(x, \xi, t) = F_A(t), \quad (1)$$

and the second moment yields the relationship

$$\int_{-1}^1 dx x H_A^f(x, \xi, t) = M_2^{f/A}(t) + \frac{4}{5} \xi^2 d_A^f(t) \quad (2)$$

which constrains the  $\xi$ -dependence of the GPDs. At  $t \rightarrow 0$ , the first term of the right-hand side of Eq. (2) is the momentum fraction of the target carried by a given quark. The second term of Eq. (2) is the so-called  $D$ -term which was shown to encode information about the spatial distribution of forces experienced by quarks and gluons inside hadrons [39].

DVCS is the simplest process to access GPDs. At leading order (Fig. 5), this mechanism corresponds to the absorption of a virtual photon by a quark carrying the longitudinal momentum fraction  $x + \xi$ . The struck quark emits quasi-instantaneously a real photon and goes back into the nuclear system with the longitudinal momentum fraction  $x - \xi$ . The important feature of this representation is the factorization [43,44] of the reaction amplitude in a known hard part corresponding to the photon-quark interaction and an unknown soft part related to GPDs. The amplitude for this process involves an integral over the intermediate quark momentum fraction  $x$  (also called Compton form factor) [15]

$$\begin{aligned} \mathcal{T}_{DVCS} \propto \sum_f e_f^2 \mathcal{P} \int_{-1}^{+1} dx \left( \frac{1}{x - \xi} \pm \frac{1}{x + \xi} \right) GPD^f(x, \xi, t) \\ - i\pi \sum_f e_f^2 \left[ GPD^f(\xi, \xi, t) \pm GPD^f(-\xi, \xi, t) \right] \end{aligned} \quad (3)$$

where  $e_f$  is the quark charge in unit of the elementary charge. The imaginary part of the DVCS amplitude appears then related to the value of the GPDs at  $x = \pm \xi$  while the real part accesses the integral of GPDs weighted by the quark propagators.

### 3.2 Beam Spin Asymmetry

The DVCS amplitude interferes with the Bethe-Heitler (BH) amplitude where the real photon is emitted either by the incoming or the scattered electron (Fig. 6). Though these processes are indistinguishable, the BH process is known and exactly calculable from the electromagnetic form factors. Furthermore, their different sensitivity to the polarization of the beam or the target

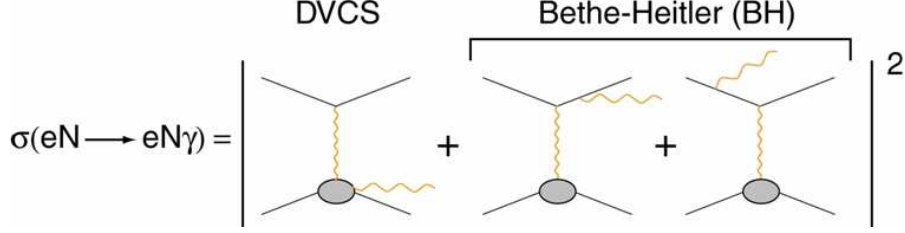


Fig. 6. The different amplitudes for electroproduction of photons.

can also be advantageously exploited. For instance, the differential cross section for a longitudinally polarized beam ( $\lambda$ ) and an unpolarized target can be expressed as [14]:

$$\frac{d^5\sigma^\lambda}{dx_A dQ^2 dt d\phi_e d\phi} = \frac{\alpha^3}{16\pi^2} \frac{x_A y^2}{Q^4 \sqrt{1+\epsilon^2}} \frac{\mathcal{T}_{BH}^2 + |\mathcal{T}_{DVCS}^\lambda|^2 + \mathcal{I}^\lambda}{e^6}, \quad (4)$$

where  $\mathcal{I}^\lambda$  represents the BH·DVCS interference amplitude, with  $y = p \cdot q / p \cdot k$  and  $\epsilon = 2x_A M_A / Q$ ,  $k$  being the incident electron 4-momentum. The different amplitudes can be written as:

$$\mathcal{T}_{BH}^2 = \frac{e^6 (1+\epsilon^2)^{-2}}{x_A^2 y^2 t \mathcal{P}_1(\phi) \mathcal{P}_2(\phi)} \sum_{n=0}^{n=2} c_n^{BH} \cos(n\phi), \quad (5)$$

$$|\mathcal{T}_{DVCS}^\lambda|^2 = \frac{e^6}{y^2 Q^2} \sum_{n=0}^{n=2} \left\{ c_n^{DVCS} \cos(n\phi) + \lambda s_n^{DVCS} \sin(n\phi) \right\}, \quad (6)$$

$$\mathcal{I}^\lambda = \frac{e^6}{x_A y^3 t \mathcal{P}_1(\phi) \mathcal{P}_2(\phi)} \sum_{n=0}^{n=3} \left\{ c_n^{\mathcal{I}} \cos(n\phi) + \lambda s_n^{\mathcal{I}} \sin(n\phi) \right\}, \quad (7)$$

where the BH and interference amplitudes contains an additional  $\phi$ -dependence arising from the BH propagators, as opposed to the squared DVCS amplitude. At leading order of the coupling constant and twist-2 dominance, the coefficients  $c_0^{DVCS}$ ,  $c_1^{\mathcal{I}}$ , and  $s_1^{\mathcal{I}}$  are the only remaining ones in Eq. (6) and Eq. (7). The full expression of the different Fourier coefficients is given in Appendix A. In the case of a scalar target, the twist-2 coefficients are proportional to the real and imaginary part of the Compton form factor  $\mathcal{H}_A$  involving the chirally-even twist-2 GPD  $H_A$  [14,45].

The BSA for two opposite helicities of a longitudinally polarized electron beam can be written at the leading twist:

$$A_{LU} = \frac{x_A (1+\epsilon^2)^2}{y} s_1^{\mathcal{I}} \sin(\phi) \left/ \left[ \sum_{n=0}^{n=2} c_n^{BH} \cos(n\phi) + \frac{x_A^2 t (1+\epsilon^2)^2}{Q^2} P_1(\phi) P_2(\phi) c_0^{DVCS} + \frac{x_A (1+\epsilon^2)^2}{y} [c_0^{\mathcal{I}} + c_1^{\mathcal{I}} \cos(\phi)] \right] \right. \quad (8)$$

For a spin zero target, this expression can be rearranged according to:

$$A_{LU} = \frac{\alpha_0(\phi)\Im_A}{\alpha_1(\phi) + \alpha_2(\phi)\Re_A + \alpha_3(\phi)(\Re_A^2 + \Im_A^2)}, \quad (9)$$

where  $\Im_A = \Im\{\mathcal{H}_A\}$ ,  $\Re_A = \Re\{\mathcal{H}_A\}$  are the unknown imaginary and real parts of the Compton form factor and the  $\alpha_i(\phi)$ 's are  $\phi$ -dependent kinematical factors (Appendix A). Therefore, for a given experimental bin in  $(Q^2, x_B, t)$ , a two parameter-fit of the  $\phi$ -dependence of the BSA yields a model-independent measurement of the real and imaginary parts of the Compton form factor.

## 4 Experimental Overview

The study of nuclear DVCS is only just beginning. The deuterium was investigated at HERMES [32] and JLab Hall A [33], and the HERMES experiment was the only one to study heavier nuclei ( $^4\text{He}$ , N, Ne, Kr, and Xe) [32]. In the latter, the DVCS process was measured by identifying the scattered lepton and the real photon in the forward spectrometer. Sizable asymmetries (Fig. 7) have been reported in the missing mass region  $-1.5 < M_X < 1.7$  GeV mass, while they generally vanish at higher masses [32].

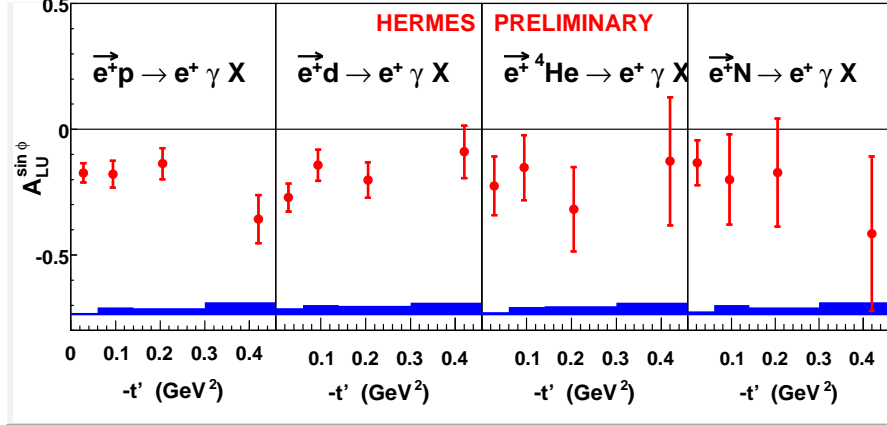


Fig. 7. The  $t$ -dependence of the BSA on  $^1\text{H}$ ,  $^2\text{H}$ ,  $^4\text{He}$ , and  $^{14}\text{N}$  expressed in terms of the coefficient  $A_{LU}^{\sin(\phi)}$  of the  $\sin(\phi)$  contribution to  $A_{LU}$  [32]; we note that in the context of the HERMES fitting procedure  $A_{LU}^{\sin(\phi)} \equiv A_{LU}$  i.e. the denominator of Eq. (8) was neglected.

These asymmetries are further separated into coherent and incoherent asymmetries taking advantage of the different  $t$ -dependence of the electromagnetic form factors: in the  $^4\text{He}$  case, for example, the coherent channel was found to dominate below  $-t = 0.05$  GeV $^2$ . The selection of the different regions in  $t$  (below and above) is then used to define coherent enriched and incoherent enriched data samples. The  $A$ -dependence of the ratio of the nuclear BSA to

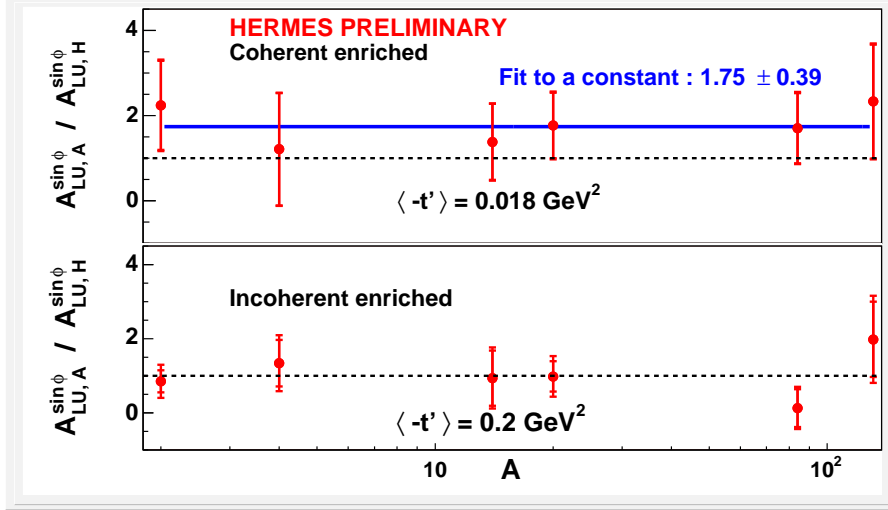


Fig. 8. The  $A$ -dependence of the ratio of the BSA on a nuclei to the BSA on the proton for the coherent enriched (upper panel) and incoherent enriched (lower panel) data samples [32].

the proton BSA is shown on Fig. 8. Within the precision of the measurements, no obvious  $A$ -dependence of the BSA is observed: the coherent enriched ratio exhibits  $\sim 2\sigma$  deviations from unity, consistent with the predictions of different models [8,34,45]; the incoherent enriched ratio is compatible with unity as one would expect from an impulse approximation approach [34].

These data clearly suffer from a lack of statistics and resolution which are mandatory for a comprehensive investigation of their physics content. Nevertheless, they clearly indicate a positive existence of a strong nuclear DVCS signal, especially in the region of interest to this proposal. In our experiment, the exclusivity of the coherent and incoherent DVCS channels will be ensured by the detection of the recoil  ${}^4\text{He}$  or nucleon in coincidence with the scattered electron and the produced real photon. Together with higher statistics ( $\sim 150$  times the highest HERMES integrated luminosity for nuclear DVCS) and simpler nature of  ${}^4\text{He}$ , these measurements will allow quantitative investigation of nuclear DVCS.

## 5 Experimental Setup

We are proposing to measure DVCS beam spin asymmetries on  ${}^4\text{He}$  using the 6 GeV highly polarized electron beam of CEBAF. The experiment will benefit from the unique opportunity offered by the combination of the CLAS, the radial time projection chamber (RTPC), and the inner calorimeter (IC) detectors. This association allows for the cleanest identification of coherent DVCS on  ${}^4\text{He}$  by detecting all the reaction products of the process  $e^4\text{He} \rightarrow e\gamma^4\text{He}$ :

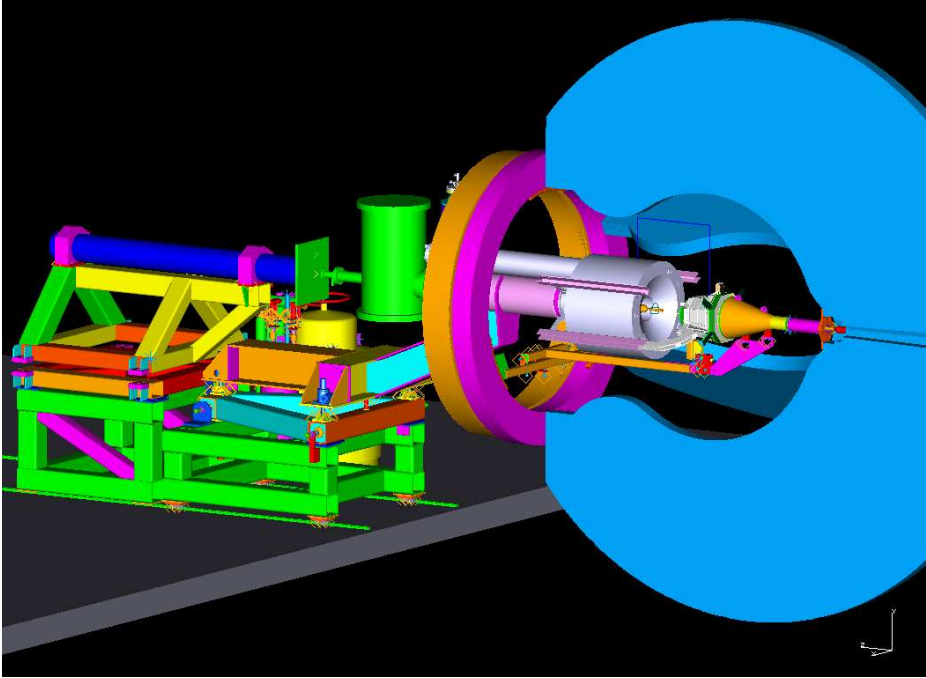


Fig. 9. Proposed configuration for the CLAS detector similar to the CLAS approved experiment E07-009 [46].

namely the scattered electron (CLAS), the produced real photon (IC+CLAS), and the recoil nucleus (RTPC). Incoherent DVCS will also be studied via semi-exclusive reaction  $e^4\text{He} \rightarrow e\gamma pX$ , where instead of  $^4\text{He}$  a proton will be detected in CLAS detector.

### 5.1 CLAS Setup

The essential requirements for the proposed experiment are:

- the detection of electrons at relatively high  $Q^2 > 1 \text{ GeV}^2$  and  $W > 2 \text{ GeV}$ ;
- the detection of real photons at small angles with respect to the virtual photon momentum  $\vec{q}$ ;
- the detection of the low momentum recoiling  $\alpha$  particles at  $|\vec{p}'| > 0.27 \text{ GeV}$  for the coherent channel;
- the detection of the struck proton in the incoherent DVCS.

These objectives will be achieved by configuring the CLAS detector in an arrangement similar to the recently completed E01-113 (e1-DVCS) experiment [47], and identical to the arrangement (Fig. 9) of the CLAS approved experiment E07-009 [46]. This setup includes the standard detector packages of the six CLAS sectors: drift chambers, time-of-flight scintillators, Čerenkov detectors, and electromagnetic calorimeters. A radial time projection cham-

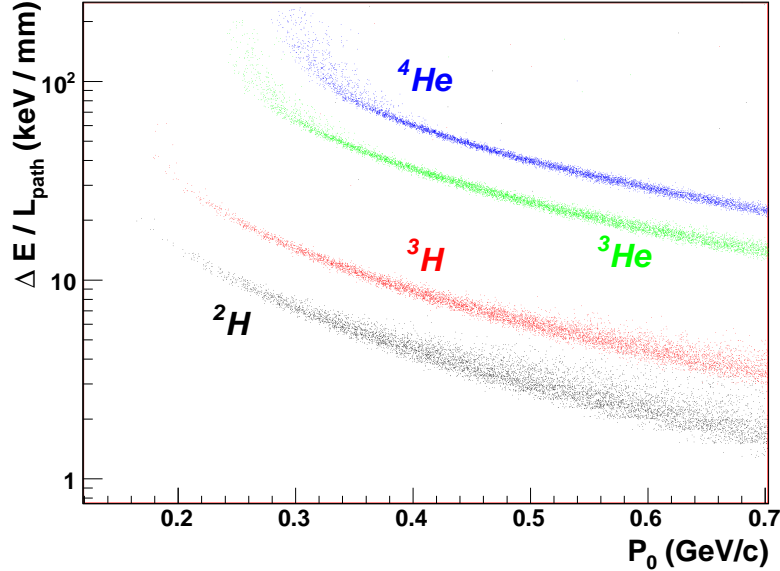


Fig. 10. Average energy loss rate  $dE/dx$  in the sensitive volume of BoNuS RTPC versus momentum for various nuclei from a GEANT4-based detector simulation program (adapted from Ref. [46]).

ber for recoil particles detection and the inner calorimeter for real photons detection will complement the configuration. Similarly to e1-DVCS [47] and BoNuS [48], the use of a solenoid magnet instead of the CLAS mini-torus shields IC and the Region I of the CLAS drift chambers from the Möller electron background. In order to reduce the ionization losses of the recoiling  $\alpha$ , and consequently lower the  $t$  detection threshold, a thin gaseous target similar to the one used in the BoNuS experiment is foreseen.

## 5.2 BoNuS RTPC

The low momentum  $\alpha$ -particles will be detected with the already existing RTPC which was originally designed for the BoNuS experiment [48]. It is a 20 cm long barrel with a 3 cm and 6 cm inner and outer radii, respectively. This detector allows for determination of the trajectory of the low momentum particles and the measurement of their energy loss rate while crossing through the sensitive volume filled with gas. The energy loss rate is the key-quantity for the identification of the particles nature: a good separation of deuteron, triton,  ${}^3\text{He}$  and  ${}^4\text{He}$  is expected in the momentum range of interest for this experiment (Fig. 10).

This radial time projection chamber performed successfully during the BoNuS experiment, whose data analysis is currently in an advanced stage. For example, Fig. 11 (left) shows the correlation between the  $z$ -vertex positions as determined from CLAS and the time projection chamber. The momentum of the spectator proton determined from the RTPC was used to correct for the

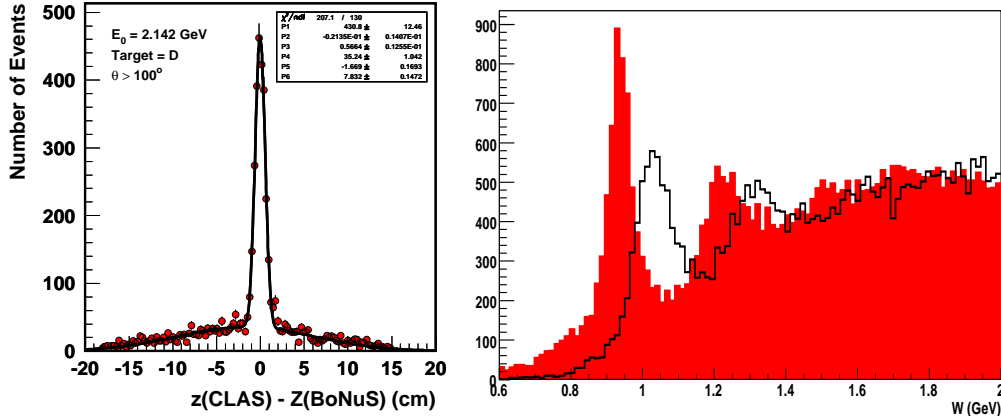


Fig. 11. Difference between the  $z$ -vertex positions determined by CLAS and BoNuS tracking for electron and proton, respectively [46] (left); distribution of the neutron mass before (black line) and after proton momentum from RTPC is taken into account (in red).

Fermi motion leading to a remarkable improvement of the neutron peak in the  $d(e, e'p)n$  reaction, as illustrated in Fig. 11 (right). The black histogram shows the missing mass distribution calculated assuming a neutron target for events where electron and the proton are detected, but without using the proton momentum from RTPC. The red filled histogram shows the neutron mass distribution as the missing mass in the  $d(e, e'p)n$  reaction using RTPC information. The position of the peak is closer to the correct neutron mass value, and the width of the peak significantly decreases once the spectator proton is tagged and its momentum is taken into account.

In the context of this proposal, the main issue of the BoNuS run was the limited event rate of  $\sim 500$  Hz from the RTPC, setting the limit for the whole data acquisition system. This limitation originates from the current readout controller of the RTPC, which does not support the eight buffer pipeline mode. This controller is not the standard for the front end cards which were purchased from CERN. We plan to remove this limitation by using the standard readout controller of ALICE TPC front end cards, which would increase the readout rate above 2 kHz. The details of the proposed modifications are discussed in Appendix B.

### 5.3 Internal Calorimeter

The forward calorimeter of CLAS allows for photon detection down to angles of  $15^\circ$ , which is not low enough if one wants to access small  $-t$  range. CLAS detector can be augmented with an electromagnetic calorimeter able to detect photons down to polar angles of  $4^\circ$ . Such a calorimeter has been constructed and was used during E01-113 experiment [47]. This detector consists of 424

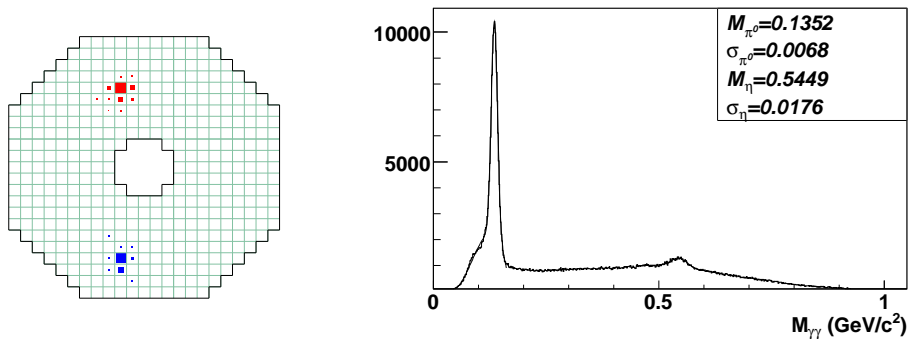


Fig. 12. An example of a two-cluster event in the Inner Calorimeter (left), and the invariant mass distribution of two photons detected in IC (right).

PbWO<sub>4</sub> crystals arranged in a projective geometry. During e1-DVCS experiment three final state particles were detected: the electron and the proton in CLAS, and the photon in the forward calorimeter or Inner Calorimeter. The calorimeter performed very well without showing signs of significant radiation damage during 35 days of running at the achieved luminosity of  $\sim 2 \times 10^{34} \text{cm}^{-2} \text{s}^{-1}$ . The energy calibrations of the calorimeter were performed using two-cluster events from  $\pi^0$  decays [49]. Figure 12 (left) shows the two clusters in the IC from a neutral pion decay. The mass resolution for two photon events can be seen in Fig. 12 (right). After combining the results of the calibrations from pion decays [49] with the information from the GEANT-based simulation [50] a parametrization of the energy resolution was achieved:

$$\frac{\sigma_E}{E} \sim \frac{1.9}{E} \oplus \frac{3.3}{\sqrt{E}} \oplus 2.4 . \quad (10)$$

The position resolution of IC estimated from simulation [50] was consistent with the data, and can be parametrized as:

$$\sigma_x = \sigma_y = \frac{1.8}{\sqrt{E}} , \quad (11)$$

where energy is measured in units of GeV and the position is in  $mm$ . This translates into  $\sim 0.7$  mrad for our experimental setup.

The time resolution of the IC was determined by comparing the vertex times of the scattered electron and the photon [51]. The obtained resolution of 0.7 ns is enough to reject the accidental coincidences between CLAS and IC.

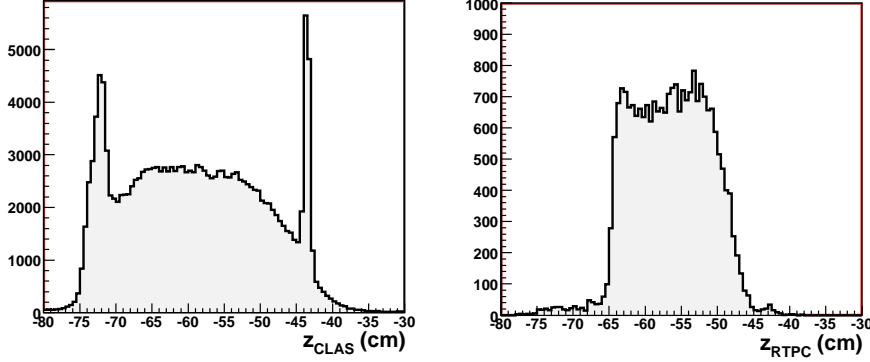


Fig. 13. Distribution of events versus  $z$ -coordinate of the tracks: electrons detected and reconstructed in CLAS are on the left panel; charged particles in RTPC are on the right panel.

#### 5.4 Beamline

The proposed experiment requires highly polarized electron beam incident on a  ${}^4\text{He}$  target. The amount of target material on the path of the recoil helium nucleus should be small to allow for its detection. To accomplish this we will use a  $\sim 20$  cm long thin gaseous target at 7 atm pressure, similar in design to the one used in BoNuS experiment. The distributions of the vertex  $z$ -coordinate from CLAS and RTPC from BoNuS data are shown in Fig. 13. The left panel is for electrons detected and reconstructed in CLAS, the right panel is for tracks in RTPC. The peaks in the left panel of Fig. 13 are from the upstream and downstream target windows. We estimate that  $\sim 15\%$  of the triggers will originate in the target inlet and exit windows, while the contributions from these windows in the RTPC will be negligible (Fig. 13 right). With such a target we can achieve a luminosity of  $L \approx 1.2 \times 10^{34} \text{cm}^{-2} \text{s}^{-1}$  for nucleons with  $I_B \approx 130$  nA electron beam current. Further increase of the beam intensity may result in higher levels of accidental background in CLAS and RTPC, which can be detrimental for the data analysis of non-exclusive reactions.

In order to prevent the Hall-B Faraday Cup from damage we will shield it with the beam blocker used during BoNuS experiment. The beam intensity will be measured using the Hall-B beam position monitors (BPM) and synchrotron light monitor (SLM). The SLM will also be used for the online monitoring of the beam charge asymmetry. We will use the standard Hall B Möller polarimeter to measure the electron beam polarization approximately once per week, or whenever the beam conditions change.

## 5.5 Trigger

The trigger configuration for the proposed experiment will be a regular CLAS trigger routinely used for electron runs. This trigger will require a coincidence between CLAS electromagnetic calorimeter and the Čerenkov Counter within a sector, which will initiate the read-out of all CLAS components, IC, and RTPC. Scaling the e1-DVCS trigger rate at luminosity  $L = 1.5 \times 10^{34} \text{ cm}^{-2}\text{s}^{-1}$  we estimate that the trigger rates at the nucleon luminosity  $L = 1.2 \times 10^{34} \text{ cm}^{-2}\text{s}^{-1}$ , corresponding to 130 nA beam current, would be 1.7 kHz with the discriminator threshold settings used in e1-DVCS. Studies during CLAS e6a running period showed that by raising the thresholds for the Čerenkov Counters from 20 mV to 100 mV, which corresponds to an increase of the detection threshold from 0.2 photoelectrons to 1 photoelectron, one can reduce the CLAS trigger rate by  $\sim 30\%$ . The typical electron identification cuts in the CLAS data analyses are larger than two photoelectrons (for example see Ref. [52]). Therefore, a single photoelectron trigger threshold for the Čerenkov Counters will not have a significant impact on the final results, especially for the measurements of asymmetries, where the detector efficiencies cancel to the first order. The expected rate with the proposed trigger at the beam current of 130 nA is  $\sim 1.1$  kHz.

The CLAS data acquisition system allows for up to eight trigger bits to be included in the trigger. Because we propose to run this experiment in parallel with E07-009, the two experiments can use separate independent trigger bits. The trigger rate for E07-009 setup at 130 nA beam current was estimated to be  $\sim 1$  kHz [46]. In the case when the two triggers are mutually exclusive, the total trigger rate will be equal to the sum of the rates of the trigger bits. Therefore, the combined trigger rate for this experiment and for E07-009 will approximately be 2 kHz.

## 6 Measurements

The analysis procedures to measure the beam spin asymmetries for coherent and incoherent DVCS on  $^4\text{He}$  is described in this section. For all events the scattered electron and the real photon will be detected. For the coherent production, we require in addition the detection of the recoiling  $^4\text{He}$  nucleus while for the incoherent case the detection of a proton is necessary.

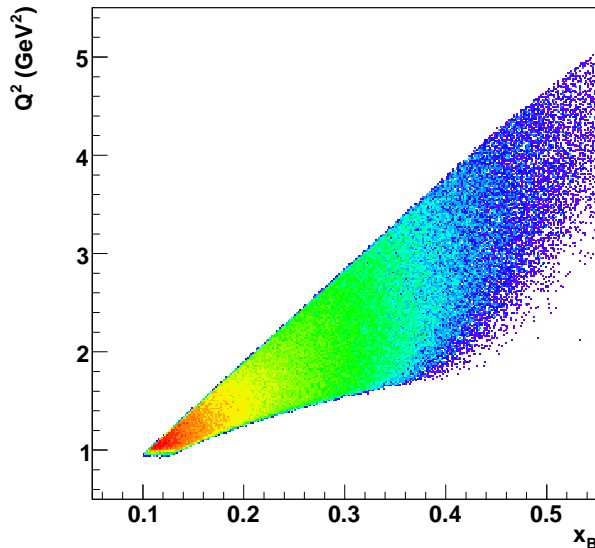


Fig. 14. Correlation between  $x_B$  and  $Q^2$  for DVCS process on  ${}^4\text{He}$  ( $z$ -axis in logarithmic scale).

### 6.1 Kinematic Coverage

DCVS is the hard exclusive production of a real photon in lepton scattering,

$$e(k) + P(p) \rightarrow e(k') + P(p') + \gamma(q'), \quad (12)$$

where  $k(k')$  is the four-momentum of the incoming (outgoing) electron.  $p(p')$  is the four-momentum of the initial (final) hadron. In our case the initial hadron is  ${}^4\text{He}$  nucleus. The final hadron is  ${}^4\text{He}$  for coherent reaction and it is a proton for the incoherent one. The exchanged virtual photon is described by the four-momentum  $q = k - k'$ . The photon virtuality is  $Q^2 = 4EE' \sin^2(\theta/2)$ , where  $E$  and  $E'$  are the energy of the incoming and outgoing electron respectively. The invariant mass of the system of the virtual photon and proton is:

$$W^2 = (q + p)^2 = M_p^2 + 2M_p\nu - Q^2, \quad (13)$$

where  $\nu$  is the energy of the virtual photon. The four-momentum transfer to the nucleon or nucleus is:

$$t = (p - p')^2 = (q - q')^2. \quad (14)$$

Other variables of interest are  $x_B = \frac{Q^2}{2M_p\nu}$ ,  $\phi$  the angle between the lepton scattering angle and photon production plane, and  $\theta_{\gamma^* \gamma}$  the angle between virtual and real photon. The kinematical cuts on the detected lepton are:

- In order to be in the hard scattering regime, we require that  $Q^2 > 1 \text{ GeV}^2$ .

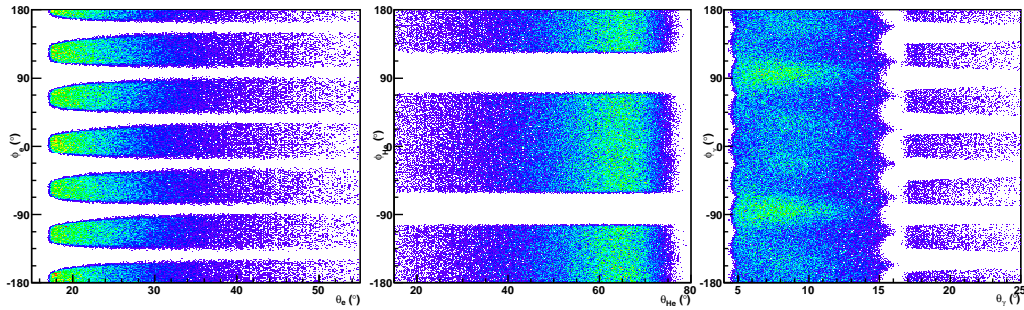


Fig. 15.  $\varphi$  and  $\theta$  laboratory frame angles for all detected particles in coherent DVCS off  ${}^4\text{He}$ . From left to right: electron,  ${}^4\text{He}$  and the real photon.

- The invariant mass of the virtual photon-proton system is required to be larger than 2 GeV.

All three main components required for this experiment - CLAS, IC and RTPC, have been implemented into a GEANT-based detector simulation code GSIM. Although it successfully describes the main properties of these detectors, it takes more than one second to simulate a single CLAS event, which sometimes makes the usage of this program impractical. Using the experimental data and the simulated data from GSIM a simplified code, FastMC, has been developed for a quicker way of determining the detector response for particular reactions. This code incorporates the geometrical acceptance of the detectors as well as a parametrization of the resolutions of each component. We used this program to determine the detector response for the proposed measurements.

Figure 14 shows the correlation between  $x_B$  and  $Q^2$  variables which are determined by the acceptance of CLAS for electrons. Figure 15 shows the correlation between the azimuthal angle  $\varphi$  and the polar angle  $\theta$  in the laboratory frame for all detected particles in the coherent DVCS off  ${}^4\text{He}$ . The electron is detected in CLAS. Its  $\varphi$  and  $\theta$  distributions show the six CLAS sectors.

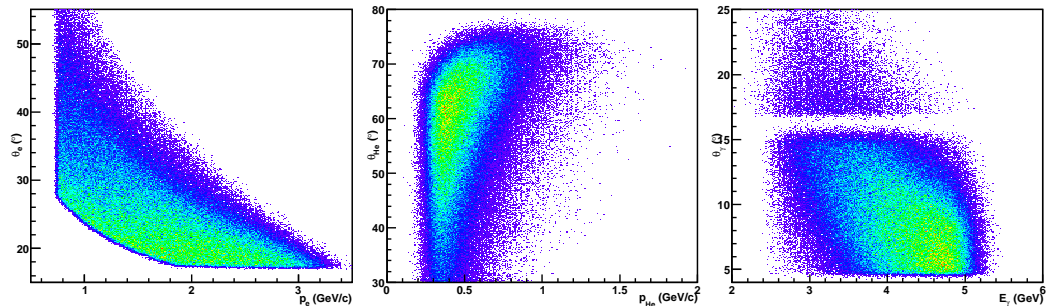


Fig. 16. The correlation between the momentum and the scattering angle in the laboratory frame for all detected particles in coherent DVCS off  ${}^4\text{He}$ . From left to right: electron,  ${}^4\text{He}$  and the real photon.

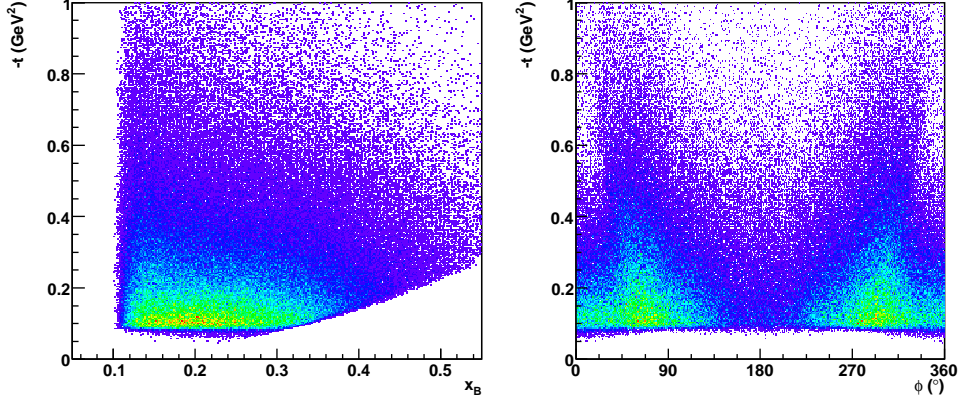


Fig. 17. The correlations between the transfer momentum  $-t$  and  $x_B$  (left) and the transfer momentum  $-t$  and the azimuthal angle  $\phi$  (right) in coherent DVCS off  ${}^4\text{He}$ .

The recoil  ${}^4\text{He}$  is detected in the time projection chambers. Its  $\varphi$  and  $\theta$  distributions show the two half-cylinders of the RTPC. Photons emitted at angles below  $15^\circ$  are detected with IC, while those which are emitted at larger angles are detected in CLAS electromagnetic calorimeter. The CLAS coverage for coherent DVCS process on  ${}^4\text{He}$  in terms of momentum of the detected particles and their azimuthal angle  $\theta$  in the laboratory frame is shown in Fig. 16. The horizontal gap in the right panel of Fig. 16 corresponds to the gap in the angular coverage of the CLAS forward calorimeter and IC.

The correlation between the transfer momentum  $t$ , the azimuthal angle  $\phi$  and  $x_B$  is shown in Fig. 17. The minimum value of  $-t \sim 0.07 \text{ GeV}^2$  in Fig. 17 is determined by the minimum momentum of detection  $p_{min} = 0.27 \text{ GeV}$  for the recoil  ${}^4\text{He}$ . The two enhancements in the  $\phi$  angle on the right panel of Fig. 17 are due to two half-cylinders of the BoNuS RTPC separated by a small azimuthal gap.

Since we are detecting all produced particles, we can assume that the missing mass squared  $M_x^2 = (q + p - q')^2$  is equal to the mass of  ${}^4\text{He}$ . Therefore, it is possible to calculate the four-momentum transfer  $t$  without the knowledge of the photon energy  $E_\gamma$ . The result is called constrained momentum transfer  $t_c$  which can be written as:

$$t_c = \frac{-Q^2 - 2\nu(\nu - \sqrt{\nu^2 + Q^2} \cos \theta_{\gamma^*\gamma})}{1 + \frac{1}{M_p}(\nu - \sqrt{\nu^2 + Q^2} \cos \theta_{\gamma^*\gamma})} \quad (15)$$

The difference between the generated momentum transfer  $t$  and the reconstructed  $t_c$  is of the order of 5% as shown in Fig. 18 along with the resolutions for  $Q^2$ ,  $x_B$  and  $\phi$ .

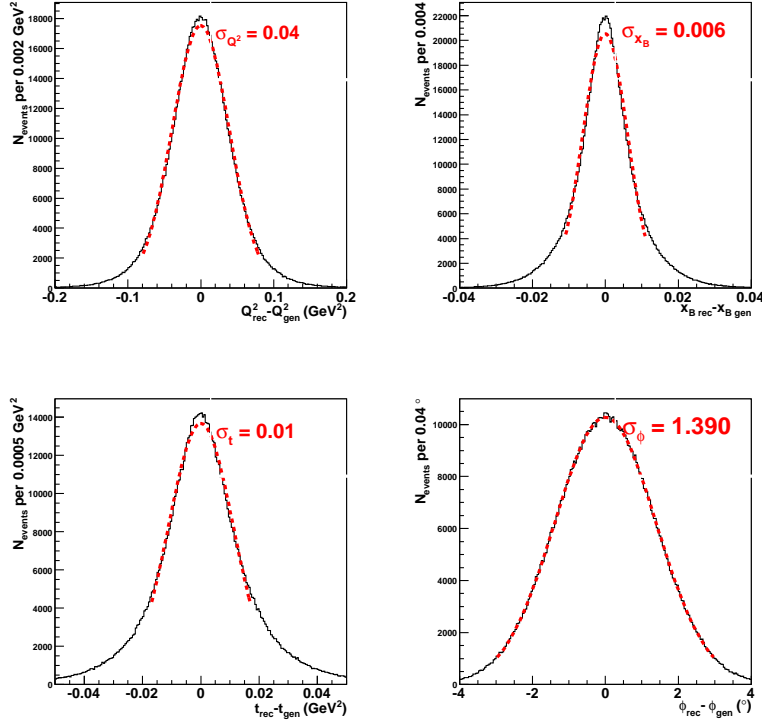


Fig. 18. CLAS resolution for kinematic quantities  $Q^2$ ,  $x_B$ ,  $t$  and  $\phi$ .

## 6.2 Exclusivity

In order to access the beam spin asymmetry, one needs to identify exclusive DVCS-BH events. To ensure exclusivity, only events with a good electron, one real photon and a recoiling  ${}^4\text{He}$  are selected as coherent events. Those with a good electron, one real photon and one proton are selected as incoherent events. To reduce even more the contribution of non-exclusive events, the following kinematical cuts have to be applied:

- Considering the “particle”  $X$  in the processes  $e {}^4\text{He} \rightarrow e' {}^4\text{He} \gamma X$  and  $e {}^4\text{He} \rightarrow e' p \gamma X$  its transverse missing momentum ( $\Delta P_x, \Delta P_y$ ) is calculated and required to be small, e.g.  $\sqrt{\Delta P_x^2 + \Delta P_y^2} < 0.1 \text{ GeV}$  for coherent DVCS.
- The angle between the direction of the detected photon and the expected one  $\theta_{\gamma X}$  for exclusive event is also required to be small, e.g.  $\theta_{\gamma X} < 1.75^\circ$  for coherent DVCS.
- For the exclusive reaction of interest, the three produced particles have to be coplanar. For the coherent reaction, the coplanarity angle is defined as the angle between the  $(\gamma^*, {}^4\text{He})$  and  $(\gamma, {}^4\text{He})$ . For the incoherent case the  ${}^4\text{He}$  is replaced by the proton.
- A cut on the missing energy  $\Delta E < 0.3 \text{ GeV}$  is also applied.

Figure 19 illustrates the contributions of non-exclusive events ( $\pi^0$  events) to the coherent DVCS data sample. The number of simulated  $\pi^0$  events is five times the number of the simulated single photon production events. The dependencies of the contamination from  $\pi^0$  versus the missing transverse momentum  $\Delta P_x$  and  $\Delta P_y$ , the angle  $\theta_{\gamma X}$  and the coplanarity angle ( $\theta_{\gamma\gamma^*p}$ ) are shown in different panels of Fig. 19. The black histograms are the total number of events, while the red histogram is for the events which satisfied the exclusivity conditions except for the cuts on the variable being displayed. The red vertical lines show the values of the cuts for that variable. Figure 20 illustrates the effectiveness of the exclusivity cuts on reducing substantially the contamination of the  $\pi^0$  background. The dashed curve in the missing energy plot represents the remaining  $\pi^0$  contribution after applying all the cuts discussed above.

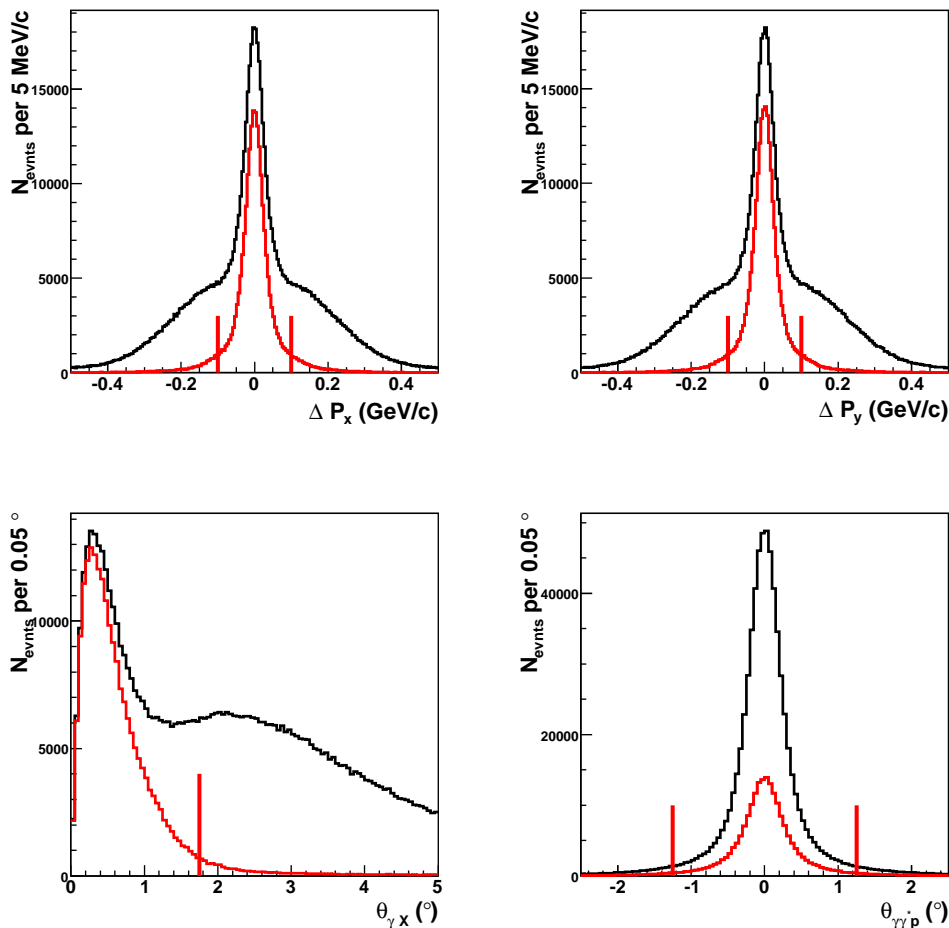


Fig. 19. Contribution of non-exclusive events ( $\pi^0$ ) to coherent DVCS. The red curve represents the exclusive events. The black curve is the sum of the contributions from exclusive and non-exclusive events. The red vertical lines show the values of the exclusivity cuts.

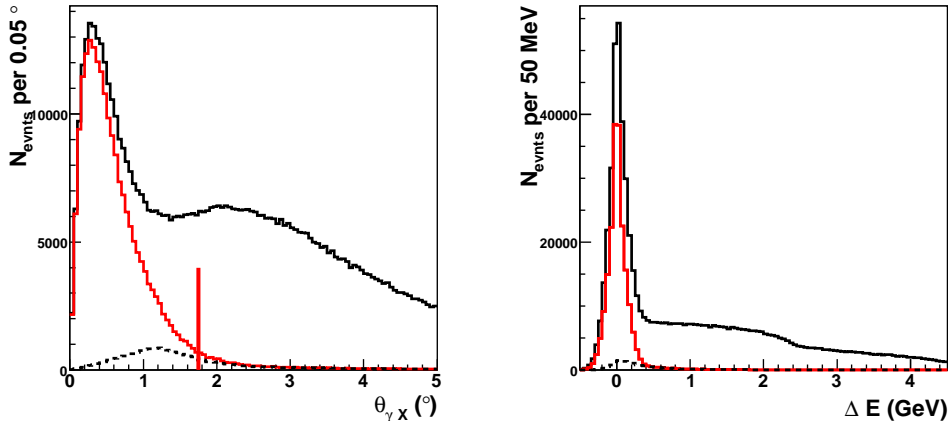


Fig. 20. Left figure is a plot of the angle  $\theta_{\gamma X}$ . The black curve represents the contribution from exclusive and non-exclusive events. The red curve results from the cuts on  $\Delta P_x$ ,  $\Delta P_y$  and the coplanarity angle ( $\theta_{\gamma\gamma^*p}$ ). The dashed curve is the remaining  $\pi^0$  contamination. Right figure is a plot of the missing energy  $\Delta E$ . The black curve is the contribution from exclusive and non-exclusive events, respectively. The red curve results from the cuts on  $\Delta P_x$ ,  $\Delta P_y$ , the coplanarity angle ( $\theta_{\gamma\gamma^*p}$ ) and  $\theta_{\gamma X}$  angle. The dashed curve is the remaining  $\pi^0$  contamination.

### 6.3 Background Subtraction

One of the issues encountered during previous DVCS experiments was the contamination from events containing a  $\pi^0$  which decayed into two photons. In such cases one of the photons can be detected, while the other one may be outside of the detector acceptance, thus mimicking a good DVCS event. The missing mass for such events will be equal to zero, the photon mass, while the cuts on the cone angle and the missing energy described in Sec. 6.1 and Sec. 6.2 will still be efficient tools to reduce the contamination from pion events. The effect of such contamination on the measured asymmetry depends on the difference between the asymmetries of the true DVCS events and  $\pi^0$  events with single detected photon. The pion contamination level in each bin needs to be identified, and the corresponding contribution into the measured asymmetry needs to be subtracted.

The analysis of e1-DVCS data to extract the beam spin asymmetries is nearly complete, and a similar pion background procedure has been used. The open trigger of CLAS allows for simultaneous detection of  $ep \rightarrow e'p\gamma$  and  $ep \rightarrow e'p\pi^0$  events, which enables us to estimate the asymmetry from  $\pi^0$  events and the contamination of the event sample. Independent data analysis conducted to estimate the asymmetry and the yields for the  $ep \rightarrow e'p\pi^0$  process greatly facilitated the background subtraction effort. The acceptances  $\mathcal{A}_{\pi^0}^{1\gamma}$  and  $\mathcal{A}_{\pi^0}^{2\gamma^0}$  for single  $\pi^0$  production events is estimated for both cases where only one pho-

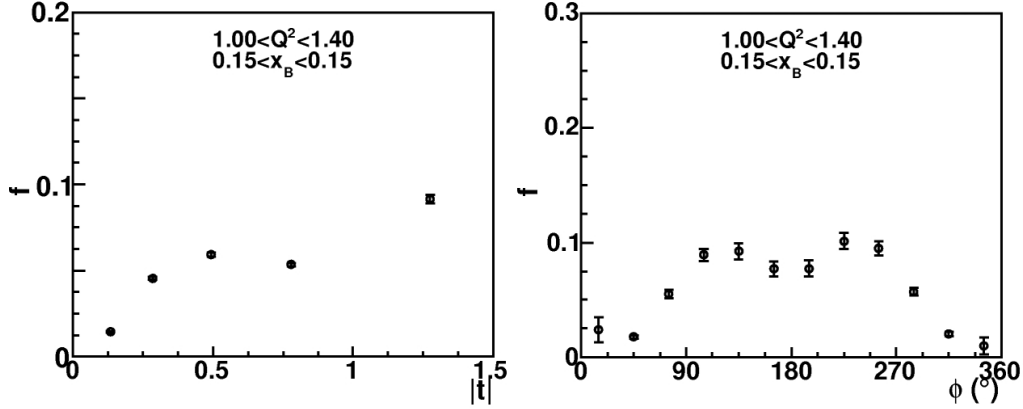


Fig. 21. Contamination factor  $f$  from  $\pi^0$  events versus four-momentum transfer  $|t|$  integrated over the photon angle  $\phi$  (left), and versus  $\phi$  (right) in the  $t$ -bin  $0.4 \text{ GeV}^2 < |t| < 0.6 \text{ GeV}^2$  as determined by e1-DVCS analysis. Both plots are for the  $(Q^2, x_B)$  bin at  $1.0 \text{ GeV}^2 < Q^2 < 1.40 \text{ GeV}^2$  and  $0.15 < x < 0.15$ .

ton and when two photons were detected using a detector simulation program. The cuts for determination of  $\mathcal{A}_{\pi^0}^{1\gamma}$  were the same as in the DVCS analysis. The cuts for estimating  $\mathcal{A}_{\pi^0}^{2\gamma}$  were taken from the analysis procedure of  $ep \rightarrow e'p\pi^0$ . The typical value for the ratio of the two acceptances determined with this method is  $\rho = \frac{\mathcal{A}_{\pi^0}^{1\gamma}}{\mathcal{A}_{\pi^0}^{2\gamma}} \sim 10 - 20\%$ . The number of single pion production events in the DVCS data sample approximately is:

$$N_{\pi^0}^{1\gamma} = \frac{\mathcal{A}_{\pi^0}^{1\gamma}}{\mathcal{A}_{\pi^0}^{2\gamma}} \times N_{\pi^0}^{2\gamma}, \quad (16)$$

where  $N_{\pi^0}^{2\gamma}$  is the number of events in the CLAS in the exactly the same data files used for the DVCS analysis.

The described procedure showed that the exclusivity cuts on the cone angle, missing mass and missing energy reduce the contamination from pion events to  $f = \frac{N_{\pi^0}}{N_{tot}} \sim 5 - 10\%$  in the kinematic range covered by the e1-DVCS experiment. The dependence of the ratio  $f$  on the four-momentum transfer  $|t|$  and photon angle  $\phi$  is shown in Fig. 21 in a fixed bin in  $Q^2$  and  $x_B$ . Subtracting the asymmetry for  $\pi^0$  events from the measured asymmetry weighted by appropriate factors yields the true asymmetry for DVCS/BH process:

$$A_{LU}^{DVCS} = \frac{1}{1-f} \left( A_{LU}^{exp} - f \tilde{A}_{LU}^{\pi^0} \right), \quad (17)$$

where  $A_{LU}^{exp}$  is the raw asymmetry for  $ep \rightarrow ep\gamma X$ , and  $\tilde{A}_{LU}^{\pi^0}$  is the asymmetry measured for  $\pi^0$  events.

Although our proposed experiment is on the nuclear target, the background subtraction procedure will be similar to the one developed by e1-DVCS. For

the incoherent DVCS process on the proton the relative amount of the single pion production contamination will be approximately the same as in e1-DVCS. Estimates of the contamination from  $\pi^0$  production to the coherent DVCS can be made based on a Regge model [53,54]. Taking into account the allowed quantum numbers and chirality of the  $t$ -channel exchanges in  $\pi^0$  production from both  ${}^4\text{He}$ , and from the proton, one sees that the latter is expected to be dominated by  $\omega$  and  $\rho$  exchanges, while only  $\omega$  exchanges can contribute in the case of  ${}^4\text{He}$ . Therefore, for a constant final state invariant mass, based on the model of [54], one expects  $\pi^0$  contamination to be reduced in  ${}^4\text{He}$  by approximately a factor of two. This reduction is even larger as the final state invariant mass increases.

#### 6.4 Extraction of Asymmetries

The polarized beam of CEBAF and the large acceptance of CLAS will allow us to extract the beam spin asymmetry  $A_{LU}$  for various bins in  $x_B$ ,  $t$ ,  $\phi$  for both coherent and incoherent DVCS processes. The beam spin asymmetry in each bin is defined as:

$$A_{LU} = \frac{1}{P_B} \frac{N^+ - N^-}{N^+ + N^-}, \quad (18)$$

where  $P_B$  is the beam polarization, and  $N^+$  and  $N^-$  are the number of events detected with positive and negative helicity of electrons, respectively. The statistical uncertainty of  $A_{LU}$  is:

$$\sigma_{A_{LU}} = \frac{1}{P_B} \sqrt{\frac{1 - (P_B A_{LU})^2}{N}}, \quad (19)$$

where  $N = N^+ + N^-$  is the total number of measured events. Therefore, it is absolutely crucial for this measurements to have a highly polarized electron beam in order to keep the statistical uncertainty low.

## 7 Beam Time Request

### 7.1 Projections

In order to estimate the CLAS acceptance and the event yields we simulated events using the Bethe-Heitler cross sections for single photon radiation process. This obviously assumes that the cross sections are dominated by the radiative emissions of photons by incoming or outgoing electron. We used the FastMC program to determine the acceptance of the detector and to project

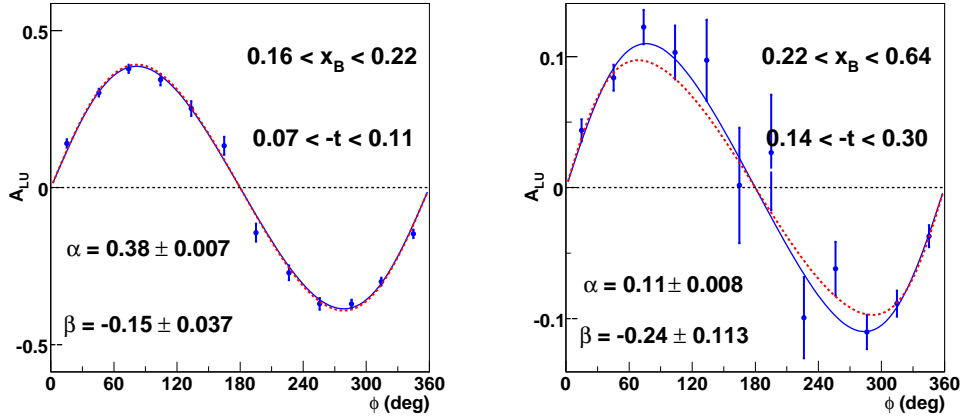


Fig. 22. Beam spin asymmetry for coherent DVCS versus  $\phi$  for two different bins of  $x_B$  and  $t$ . The solid curves are fits to the simulated data, the dashed curves are from the model by Strikman and Guzey [34].

the statistical uncertainties. The kinematic coverage in  $Q^2$ ,  $x_b$ ,  $t$  and  $\phi$  for the coherent production is shown in Figs. 14 and 17. Our ability to access the low values of momentum transfer  $-t$  will allow us to probe the DVCS kinematics where the factorization is expected to be valid and to minimize the cross section reduction due to the fast-falling electromagnetic form-factor of the  ${}^4\text{He}$  nucleus. Nearly full coverage in the  $\phi$  angle enables us to extract the Compton form-factors  $\mathcal{H}_A(x_B, t)$  by fitting the azimuthal dependence of the asymmetry.

The projected asymmetry versus  $\phi$  and the corresponding uncertainty for DVCS on  ${}^4\text{He}$  are shown in Fig. 22. The statistical error bars are calculated for 45 days at a nucleus luminosity of  $L = 3 \times 10^{33} \text{ cm}^{-2}\text{s}^{-1}$ . The assumed beam polarization is 85%, which is a typical value for the recent Hall-B Möller measurements. We used the ratio of the asymmetries between the nuclear and proton target from the model by Guzey and Strikman [34] multiplied by the preliminary parametrization for proton asymmetries from CLAS [23] when estimating the projected uncertainties. The two panels show two different bins of  $x_B$  and  $t$ . The red dashed curves in Fig. 22 are from the model by Guzey and Strikman [34] scaled by the proton asymmetries from Ref. [23]. The blue solid curves represent a fit to a function of the form:

$$A_{LU} = \frac{\alpha \sin \phi}{1 + \beta \cos \phi}. \quad (20)$$

The left and right panels in Fig. 23 show the expected precision for the asymmetry at  $\phi = 90^\circ$  for coherent DVCS on  ${}^4\text{He}$  versus  $t$  and  $x_B$ , respectively. Only the first and last bins in  $x_B$  are shown in Fig. 23 (left), representing the best and the worst statistical precision. The corresponding average  $Q^2$  values

are  $1.2 \text{ GeV}^2$  and  $2.1 \text{ GeV}^2$  (see Fig. 14). Similarly, the first and last bins in  $t$  are shown in Fig. 23 (right). The solid curve is from the model by Guzey and Strikman [34], and the dashed curves are from the model by Liuti and Taneja [8]. Both model predictions were obtained by normalizing the ratio for asymmetries for helium to proton to the preliminary data on the proton from CLAS[23]. Note that when showing the asymmetry versus one variable we do not integrate over the other one. The green points on the bottom of Fig. 23 (left) show the results from HERMES [32] on the helium target. There is an order of magnitude improvement in the precision of these data with respect to HERMES results [32]. We would like to point out that HERMES experiment could not reliably separate the coherent and incoherent contribution, and their results are completely dominated by the incoherent DVCS above  $-t > 0.1 \text{ GeV}^2$ . In contrast to the HERMES measurements, we can separate the two processes, and we will still have enough statistics to have multiple bins in  $x_B$  and  $t$  even for the coherent DVCS on  ${}^4\text{He}$ . The experimental uncertainties in Fig. 23 are smaller than the variance between the calculations which will allow us to discriminate between the two models.

We also estimated the statistical uncertainties for the ratio  $\frac{A_{LU}^{He}}{A_{LU}^p}$  for coherent DVCS on  ${}^4\text{He}$ , shown in Fig. 24. The predictions for the  $t$ -dependence of the models by Guzey and Strikman[34] (solid black curve) and by Liuti and Taneja [8] (dashed color curves) are shown on the left panel of Fig. 24. The difference between the two models are due to the nuclear binding effects, most importantly due to the presence of partonic transverse degrees of freedom, present in the latter calculation. The error bars will allow us to distinguish between the models even in the highest four-momentum transfer bin. The  $x_B$  dependence of the asymmetry ratio is shown on the right panel of Fig. 24,

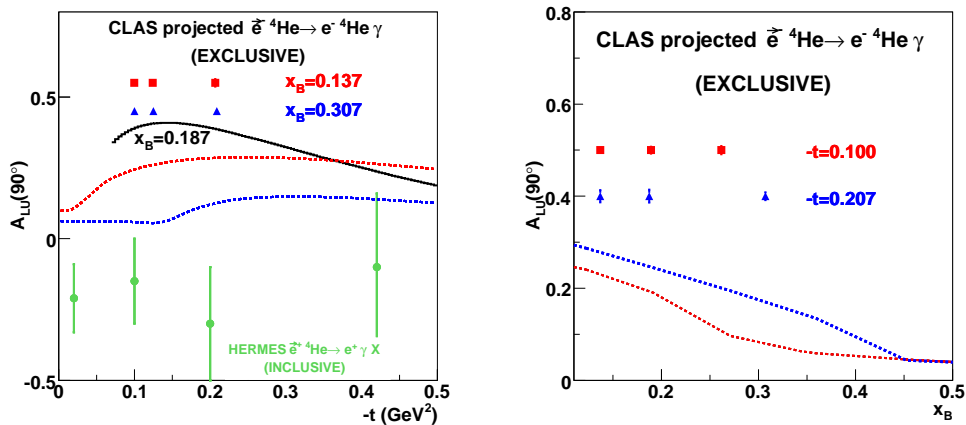


Fig. 23. Projected precision for the  $A_{LU}(90^\circ)$  for coherent DVCS on  ${}^4\text{He}$  versus  $t$  (left) and  $x_B$  (right). The black solid curve is from the model by Guzey and Strikman [34], the dashed curves are from Liuti and Taneja [8]. The HERMES results (green) are shown for comparison of the error bars.

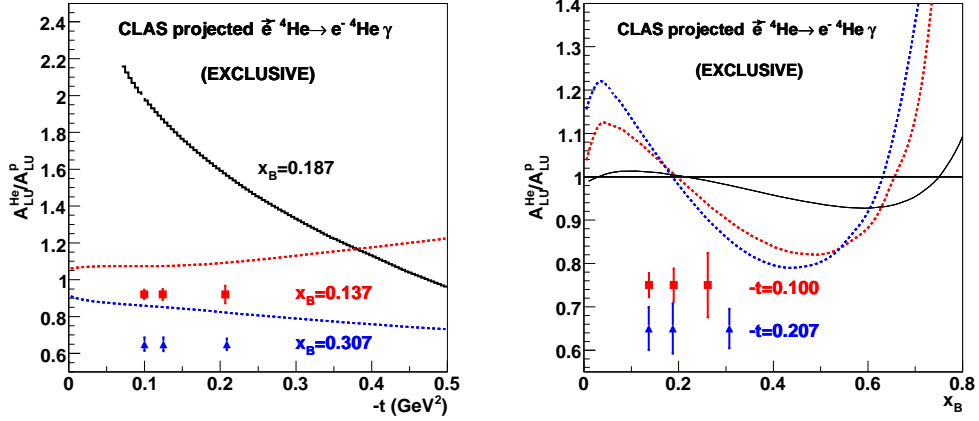


Fig. 24. Projected precision for the ratio  $\frac{A_{LU}^{He}}{A_{LU}^p}$  for coherent DVCS on  $^4\text{He}$  versus  $t$  (left) and  $x_B$  (right). The thick solid curve on the left panel is from the model by Guzey and Strikman [34], while on the right panel the thin solid curve is the calculation from Liuti and Taneja [8]. The dashed curves on both panels are from Liuti and Taneja [8].

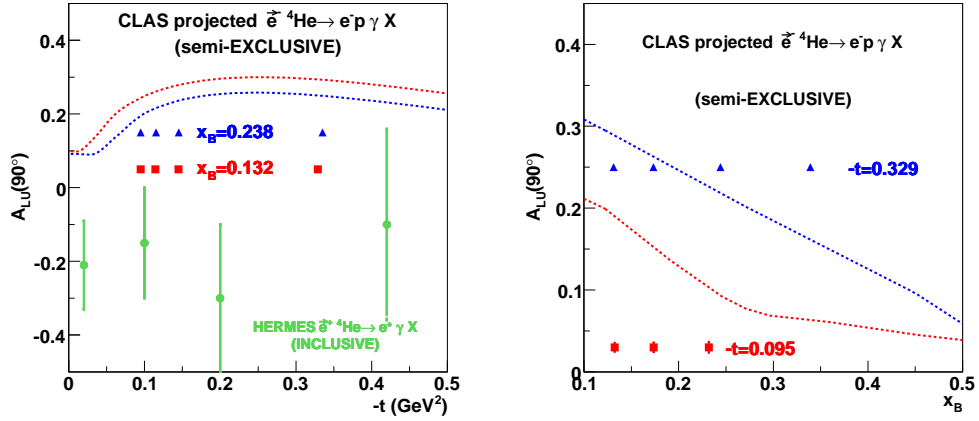


Fig. 25. Projected precision for the  $A_{LU}(90^\circ)$  for incoherent DVCS on proton versus  $t$  (left) and  $x_B$  (right). The dashed curves are from the model by Liuti [8].

where the solid black curve is the calculation by Liuti and Taneja [8] at  $t = 0$ . With increasing  $-t$  the deviations of the asymmetry ratio from 1 increases, according to the model by Liuti and Taneja [8], giving us better sensitivity to the off-shell effects. The projected error bars will allow us to see this increase in the deviations from unity both in the anti-shadowing and EMC regions.

The projected statistical precision for asymmetry for incoherent DVCS on bound proton is much higher, as can be seen in Fig. 25. The dashed curves are from the model by Liuti [8], which takes into account modifications of the hadron properties in the nuclei. The experimental uncertainties will clearly

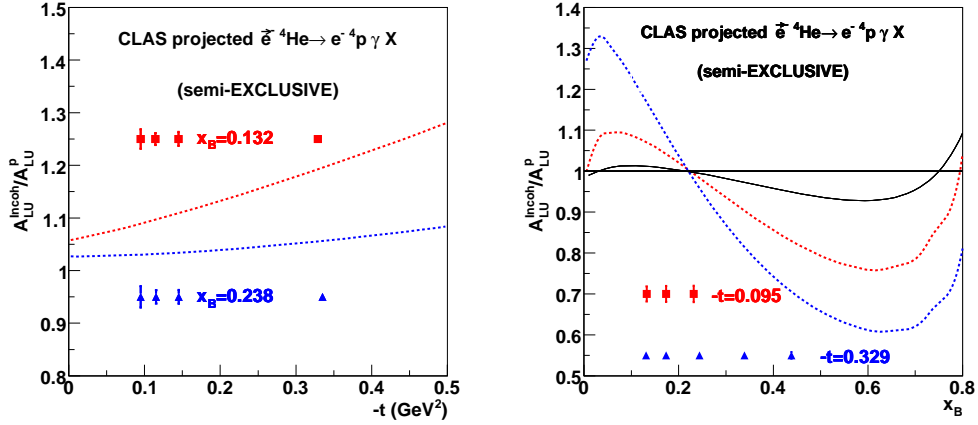


Fig. 26. Projected uncertainties for the ratio  $\frac{A_{LU}^{inc}}{A_{LU}^P}$  for incoherent DVCS on  ${}^4\text{He}$  versus  $t$  (left) and  $x_B$  (right). The dashed curves are from Liuti and Taneja [8]. The black solid curve is calculation at  $t = 0$ .

allow us to see the impact of the nuclear medium on this observable. Figure 26 shows the expected uncertainties for the ratio  $\frac{A_{LU}^{inc}}{A_{LU}^P}$  for the incoherent DVCS. The black solid line is the calculation by Liuti [8] at  $t = 0$ . The model by Guzey and Strikman[34] predicts this ratio to be equal to 1. As one can see from Fig. 26 the  $x_B$  range for the incoherent DVCS is larger than for coherent channel, extending our coverage deeper into the EMC region. Note that this is the first time that the ratios of asymmetries shown in Fig. 24 and Fig. 26 will be measured with such high precision.

## 7.2 Extraction of $\mathcal{H}_A$ Compton form factor

The beam spin asymmetry will be extracted for various bins in  $x_B$ ,  $t$  and  $\phi$ . In the twist-two approximation this quantity is only sensitive to a single GPD  $H_A(x, \xi, t)$ , and one of the main goals of this experiment is to extract the corresponding Compton form factor. By fitting the angular dependence of the measured asymmetry for coherent DVCS on  ${}^4\text{He}$  to the form given in Eq. (9) we will extract the real and imaginary parts of the Compton form-factor  $\mathcal{H}_A$ . Note that this will be the first time that both the real and imaginary parts of a nuclear Compton form-factor are extracted in a model independent way.

We conducted an exercise using the simulated pseudodata to determine the sensitivity of the proposed measurements to the real and imaginary part of the helium Compton form factor. The projected statistical uncertainties for the  $\mathcal{H}_A$  are shown in Fig. 27. The left panel shows the  $t$ -dependence and the right panel shows the  $x_B$  dependence of the Compton form factor. The dashed and solid curves are the real and imaginary parts from the model by Guzey

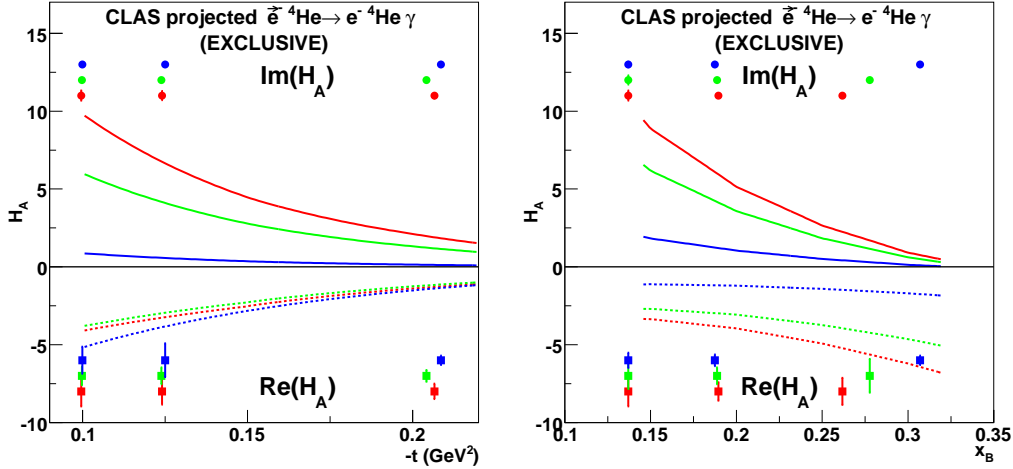


Fig. 27. Projected uncertainties for the  $\mathcal{H}_A$ . The curves are from the model by Guzey and Strikman [34]. Blue, red and green on the left panel correspond to  $x_B$  values of 0.13, 0.19, 0.28, respectively. Blue, red and green on the right panel correspond to  $-t$  values of  $0.09 \text{ GeV}^2$ ,  $0.12 \text{ GeV}^2$ ,  $0.2 \text{ GeV}^2$ , respectively.

and Strikman [34]. The squares and circles with the error bars represent the projected statistical uncertainties for the real and imaginary parts, respectively. Blue, red and green colors on the left panel correspond to  $x_B$  values of 0.13, 0.19, 0.28, respectively. the corresponding average values for the  $Q^2$  are  $1.16 \text{ GeV}^2$ ,  $1.15 \text{ GeV}^2$ ,  $2.1 \text{ GeV}^2$ , respectively (see Fig. 14). Blue, red and green colors on the right panel correspond to  $-t$  values of  $0.09 \text{ GeV}^2$ ,  $0.12 \text{ GeV}^2$ ,  $0.2 \text{ GeV}^2$ , respectively. Although the asymmetry measurement provides a better sensitivity for imaginary part, clearly, the real part of the Compton form factor can be readily extracted from the proposed measurement as well.

### 7.3 Systematic uncertainties

The main advantage of measuring beam spin asymmetries is that most of the experimental systematic uncertainties, such as acceptance, efficiencies, dead time, cancel in the ratio to the first order. Nevertheless, the uncertainties for certain quantities, such as background, beam polarization, beam charge asymmetry, still need to be accounted for.

The main source of the background for DVCS/BH events is expected to be the single  $\pi^0$  electroproduction. The kinematic cuts described in Sec. 6 will reduce the background level, and the subtraction procedure will account for the contribution from the pion events into the measured asymmetry. The e1-DVCS analysis [52] concluded that a conservative estimate for the uncertainty for pion event fraction  $\frac{\Delta f}{f} \sim 30\%$  leads to typical relative asymmetry uncertainty of  $\frac{\Delta A_{DVCS}}{A_{DVCS}} \sim 5\%$ .

Source	Systematic Uncertainty
$\pi^0$ contamination	5%
Beam polarization	3%
Acceptance	3%
Radiative corrections	1%
Beam charge asymmetry	0.3%
Total	6.6%

Table 1

Expected relative systematic uncertainties for beam spin asymmetries.

The beam polarization will be measured using the Hall-B Möller polarimeter with a precision of  $\frac{\Delta P}{P} \sim 2.5\%$ . The expected beam polarization  $P = 85\%$  will yield relative uncertainty for the asymmetry of  $\frac{\Delta A_{LU}}{A_{LU}} \sim 3\%$ .

Table 1 summarizes the expected relative uncertainties for the beam spin asymmetries. The statistical error will dominate in the bins at large  $-t$  and large  $x_B$ , while at low  $-t$  and low  $x_B$  the systematics will be the dominant contribution to the total uncertainties.

These experimental errors for the asymmetry will propagate into the extracted Compton form factor  $\mathcal{H}_A(x_B, t)$ . Also the assumption of twist-2 dominance in the fitting procedure in Sec. 7.2 will introduce additional uncertainties (known as model-dependent uncertainties). The twist-2 dominance hypothesis can be tested and the model dependence can be estimated using the same data by examining the  $Q^2$  dependence of the beam spin asymmetry and the result for the Compton form factor  $\mathcal{H}_A$ .

#### 7.4 Beam Time Request

Achieving the scientific goals presented in this proposal does not require any additional beam time in Hall-B. There is already a CLAS experiment E07-009 [46] approved to run for 45 days with 6 GeV electron beam on  $^4\text{He}$  target. That experiment will requires 130 nA electron beam incident on a 20 cm helium target, which corresponds to  $\sim 3 \times 10^{33} \text{ cm}^{-2}\text{s}^{-1}$  luminosity for nucleus. The proposed upgrade of the RTPC, which will improve the RTPC readout rate to 2 kHz, will allow the CLAS data acquisition system to handle the additional trigger rate from our experiment. Considering that the beam, target, magnet and detector configurations of E07-09 are compatible with the needs of the proposed experiment, we request to share the 6 GeV electron beamtime of 45 days with E07-009. **We also request that the electron beam be longitudinally polarized with  $P \sim 85\%$  to allow us to measure the**

**beam-spin asymmetry for coherent and incoherent DVCS processes.**

## 8 Relation to Other Experiments

This proposal is a part of the on-going experimental efforts at Jefferson Lab towards the understanding of the partonic structure of hadrons and how it is modified in the nuclear medium. It involves experimental techniques and analysis methods that were successfully applied in the previous DVCS experiments in Hall B (E01-113 [47]) and Hall A (E00-110 [55], E03-106 [56]). The proposed experiment will apply these methods to explore the totally new field of nuclear GPDs in the simplest case of the  $^4\text{He}$  nucleus. This is a fully original proposal, with no relation to any approved experiment at Jefferson Lab. The results of these measurements will set the basis for a thorough and ambitious program about nuclear GPDs at Jefferson Lab at 12 GeV.

## 9 Summary

In summary, we propose to perform an experiment in Hall B to measure the single beam spin asymmetry on a  $^4\text{He}$  target using 6 GeV polarized electron beam. Both coherent and incoherent processes will be investigated by detecting the scattered electron, photon, and either the  $^4\text{He}$  or the struck nucleon. The main objectives of these experiments are to obtain the Compton form factor  $\mathcal{H}_A(x_B, t)$  for coherent DVCS on  $^4\text{He}$ , and to measure the beam spin asymmetry  $A_{LU}$  for incoherent DVCS. These measurements, combined with the data from the DVCS on the free proton, will allow us to construct the ratios of the asymmetries for the bound and unbound protons  $R_A(x_B, t) = \frac{A_{LU}^{He}(x_B, t)}{A_{LU}^N(x_B, t)}$ . We would like to point out that this will be the first time that  $x_B$ -dependence of ratio  $R_A$ , which is the generalization of the EMC effect at non-zero momentum transfer  $t$ , will be measured. The measured beam spin asymmetries and the Compton form factor  $\mathcal{H}_A(x_B, t)$  extracted in a model-independent manner will constrain the theoretical models for the nuclear GPDs, they will provide a better insight into how the nuclear forces are distributed inside the nucleus, and how these forces deform and modify the properties of the bound nucleons, and eventually, combined with future measurements in a wider kinematic range and other observables, will lead to a three dimensional picture of the nucleus.

## 10 Appendix A

### 10.1 Bethe-Heitler propagators

The Bethe-Heitler propagators in eq. 5 and eq.7 write

$$\mathcal{P}_1(\phi) = \frac{(k - q')^2}{Q^2} = -\frac{1}{y(1 + \epsilon^2)} \left( J + 2K \cos(\phi) \right), \quad (21)$$

$$\mathcal{P}_2(\phi) = \frac{(k - \Delta)^2}{Q^2} = 1 + \frac{t}{Q^2} + \frac{1}{y(1 + \epsilon^2)} \left( J + 2K \cos(\phi) \right), \quad (22)$$

with the definitions

$$J = \left( 1 - y - \frac{y\epsilon^2}{2} \right) \left( 1 + \frac{t}{Q^2} \right) - (1 - x_A)(2 - y) \frac{t}{Q^2}, \quad (23)$$

$$K^2 = -\delta t(1 - x_A) \left( 1 - y - \frac{y^2\epsilon^2}{4} \right) \left\{ \sqrt{1 + \epsilon^2} + \frac{4x_A(1 - x_A) + \epsilon^2}{4(1 - x_A)} \delta t \right\}, \quad (24)$$

$$\delta t = \frac{t - t_{min}}{Q^2} = \frac{t}{Q^2} + \frac{2(1 - x_A)(1 - \sqrt{1 + \epsilon^2}) + \epsilon^2}{4x_A(1 - x_A) + \epsilon^2}, \quad (25)$$

where  $t_{min}$  represents the kinematical boundary of the process.

### 10.2 Fourier coefficients of a spin-0 target

The Fourier coefficients of the BH amplitude for a spin-0 target can be expressed as

$$\begin{aligned} c_0^{BH} = & \left[ \left\{ (2 - y)^2 + y^2(1 + \epsilon^2)^2 \right\} \left\{ \frac{\epsilon^2 Q^2}{t} + 4(1 - x_A) + (4x_A + \epsilon^2) \frac{t}{Q^2} \right\} \right. \\ & + 2\epsilon^2 \left\{ 4(1 - y)(3 + 2\epsilon^2) + y^2(2 - \epsilon^4) \right\} - 4x_A^2(2 - y)^2(2 + \epsilon^2) \frac{t}{Q^2} \\ & \left. + 8K^2 \frac{\epsilon^2 Q^2}{t} \right] F_A^2, \quad (26) \end{aligned}$$

$$c_1^{BH} = -8(2 - y)K \left\{ 2x_A + \epsilon^2 - \frac{\epsilon^2 Q^2}{t} \right\} F_A^2, \quad (27)$$

$$c_2^{BH} = 8K^2 \frac{\epsilon^2 Q^2}{t} F_A^2, \quad (28)$$

where  $F_A$  is the electromagnetic form factor of the nuclear target. The twist-2 coefficients of the squared DVCS amplitude writes as a function of the only one Compton form factor  $\mathcal{H}_A$  according to

$$c_0^{DVCS} = 2(2 - 2y + y^2) \mathcal{H}_A \mathcal{H}_A^*, \quad (29)$$

and the interference amplitude coefficients are

$$c_0^{\mathcal{I}} = -8(2 - y) \frac{t}{Q^2} F_A \Re\{\mathcal{H}_A\} \quad (30)$$

$$\times \left\{ (2 - x_A)(1 - y) - (1 - x_A)(2 - y)^2 \left( 1 - \frac{t_{min}}{Q^2} \right) \right\},$$

$$c_1^{\mathcal{I}} = 8K(2y - y^2 - 2) F_A \Re\{\mathcal{H}_A\}, \quad (31)$$

$$s_1^{\mathcal{I}} = 8Ky(2 - y) F_A \Im\{\mathcal{H}_A\}. \quad (32)$$

The  $\alpha_i(\phi)$  coefficients appearing in the expression of the beam spin asymmetry (eq. 8) write

$$\alpha_0(\phi) = 8Kx_A(1 + \epsilon^2)^2 (2 - y) F_A \sin(\phi), \quad (33)$$

$$\alpha_1(\phi) = c_0^{BH} + c_1^{BH} \cos(\phi) + c_2^{BH} \cos(2\phi), \quad (34)$$

$$\alpha_2(\phi) = 8 \frac{x_A}{y} (1 + \epsilon^2)^2 F_A \left[ K(2y - y^2 - 2) \cos(\phi) \right. \quad (35)$$

$$\left. - (2 - y) \frac{t}{Q^2} \left\{ (2 - x_A)(1 - y) - (1 - x_A)(2 - y)^2 \left( 1 - \frac{t_{min}}{Q^2} \right) \right\} \right],$$

$$\alpha_3(\phi) = 2 \frac{x_A^2 t}{Q^2} (2 - 2y + y^2) (1 + \epsilon^2)^2 \mathcal{P}_1(\phi) \mathcal{P}_2(\phi). \quad (36)$$

### 10.3 Fourier coefficients of spin-1/2 target

The Fourier coefficients<sup>†</sup> of the BH amplitude are

---

<sup>†</sup> In the nucleon case,  $x_A$  reduces to the usual Bjorken variable  $x_B$ , and  $M_A$  to the nucleon mass  $M_N$ ; they should be replaced accordingly in eq. 4, and eq. 23 to eq. 25.

$$c_0^{BH} = 8K^2 \left\{ \frac{Q^2}{t} (2 + 3\epsilon^2) (F_1^2 - \tau F_2^2) + 2x_B^2 (F_1 + F_2)^2 \right\} \quad (37)$$

$$\begin{aligned} &+ (2-y)^2 \left\{ (2 + \epsilon^2) \left[ \frac{\epsilon^2 Q^2}{t} \left( 1 + \frac{t}{Q^2} \right)^2 + 4(1-x_B) \left( 1 + x_B \frac{t}{Q^2} \right) \right] \right. \\ &\times (F_1^2 - \tau F_2^2) + 4x_B^2 \left[ x_B + \left( 1 - x_B + \frac{\epsilon^2}{2} \right) \left( 1 - \frac{t}{Q^2} \right)^2 \right. \\ &\left. \left. - x_B(1-2x_B) \frac{t^2}{Q^4} \right] (F_1 + F_2)^2 \right\} + 8(1 + \epsilon^2) \left( 1 - y - \frac{\epsilon^2 y^2}{4} \right) \\ &\times \left\{ 2\epsilon^2 (1 - \tau) (F_1^2 - \tau F_2^2) - x_B^2 \left( 1 + \frac{t}{Q^2} \right)^2 (F_1 + F_2)^2 \right\}, \end{aligned}$$

$$c_1^{BH} = 8K(2-y) \left\{ \left( \frac{\epsilon^2 Q^2}{t} - 2x_B - \epsilon^2 \right) (F_1^2 - \tau F_2^2) \right. \quad (38)$$

$$\left. + 2x_B^2 \left( 1 - (1 - 2x_B) \frac{t}{Q^2} \right) (F_1 + F_2)^2 \right\},$$

$$c_2^{BH} = 8K^2 \left\{ \frac{\epsilon^2 Q^2}{t} (F_1^2 - \tau F_2^2) + 2x_B^2 (F_1 + F_2)^2 \right\}, \quad (39)$$

with  $\tau = t/4M_N^2$ ;  $F_1, F_2$  are the Dirac and Pauli electromagnetic form factors of the nucleon. In the case of a nucleon target, there are four Compton form factors at leading twist [57]:  $\mathcal{H}, \widetilde{\mathcal{H}}, \mathcal{E},$  and  $\widetilde{\mathcal{E}}$ . The twist-2 coefficient of the squared DVCS amplitude is

$$c_0^{DVCS} = 2(2 - 2y + y^2) \mathcal{C}^{DVCS}(\mathcal{F}, \mathcal{F}^*), \quad (40)$$

and the interference amplitude ones write

$$c_0^{\mathcal{I}} = -8(2-y) \quad (41)$$

$$\times \Re e \left\{ \frac{(2-y)^2}{1-y} K^2 \mathcal{C}^{\mathcal{I}}(\mathcal{F}) + \frac{t}{Q^2} (1-y)(2-x_B) (\mathcal{C}^{\mathcal{I}} + \Delta \mathcal{C}^{\mathcal{I}})(\mathcal{F}) \right\},$$

$$c_1^{\mathcal{I}} = 8K(2y - y^2 - 2) \Re e \left\{ \mathcal{C}^{\mathcal{I}}(\mathcal{F}) \right\} \quad (42)$$

$$s_1^{\mathcal{I}} = 8Ky(2-y) \Im m \left\{ \mathcal{C}^{\mathcal{I}}(\mathcal{F}) \right\}. \quad (43)$$

The  $\mathcal{C}$ 's coefficients are the combinations of the nucleon Compton form factors

$$\mathcal{C}^{DVCS}(\mathcal{F}, \mathcal{F}^*) = \frac{1}{(2-x_B)^2} \left\{ 4(1-x_B) (\mathcal{H}\mathcal{H}^* + \widetilde{\mathcal{H}}\widetilde{\mathcal{H}}^*) - x_B^2 \tau \widetilde{\mathcal{E}}\widetilde{\mathcal{E}}^* \right. \quad (44)$$

$$\left. - (x_B^2 + (2-x_B)^2 \tau) \mathcal{E}\mathcal{E}^* - x_B^2 (\mathcal{H}\mathcal{E}^* + \mathcal{E}\mathcal{H}^* + \widetilde{\mathcal{H}}\widetilde{\mathcal{E}}^* + \widetilde{\mathcal{E}}\widetilde{\mathcal{H}}^*) \right\},$$

$$\mathcal{C}^{\mathcal{I}}(\mathcal{F}) = F_1 \mathcal{H} + \frac{x_B}{2-x_B} \widetilde{\mathcal{H}} - \tau F_2 \mathcal{E}, \quad (45)$$

$$\Delta \mathcal{C}^{\mathcal{I}}(\mathcal{F}) = -\frac{x_B}{2-x_B} (F_1 + F_2) \left\{ \frac{x_B}{2-x_B} (\mathcal{H} + \mathcal{E}) + \widetilde{\mathcal{H}} \right\}. \quad (46)$$

## 11 Appendix B

### 11.1 Upgrade of the RTPC readout hardware

The Radial Time Projection Chamber built for the BoNuS experiment consists of two half-cylinder TPCs, each featuring 1,600 readout pads on the outermost shell (readout plane), for a total of 3,200 pads. Groups of 16 pads are traced to a common connector on the readout plane, which supports a circuit board with 16 individual pre-amplifier channels with gain of about  $-1$ . The amplified signals are sent over a five meter long flatband cable to 128-channel receiver cards in a pseudo-VME format. The receiver cards feature  $8 \times 16$  channels of impedance-matched receiver channels, which feed the signals into the piggyback mounted Front End Cards (FECs). These readout cards are the standard readout for the ALICE TPC and were bought from CERN. The feature  $8 \times 16$  channels of pre-amplification and shaping (PASA) and eight custom ALTRO chips, providing each 16 channels of pedestal subtraction, baseline corrections, 10-bit digitization, and up to eight buffers organized in a ring structure. The receiver cards also supply the power to the amplifier/inverter cards and to the FEC. A group of 13 FEC/receiver cards is needed to read out one half-cylinder of the RTPC. The 13 cards are controlled via a data bus and a control bus by a readout controller, U2F. The U2F transmits the data via USB2.0 to a PC or VME crate controller and also provides the software download and features user-programmable output ports, like a busy feedback. At the present time, the firmware of the U2F controller does not support the eight buffer pipeline and, hence, can only be used in an event-by-event readout scheme (ROC-lock mode) when used in conjunction with the CLAS detector. This limits the DAQ rate to presently about 500 Hz. The present hardware

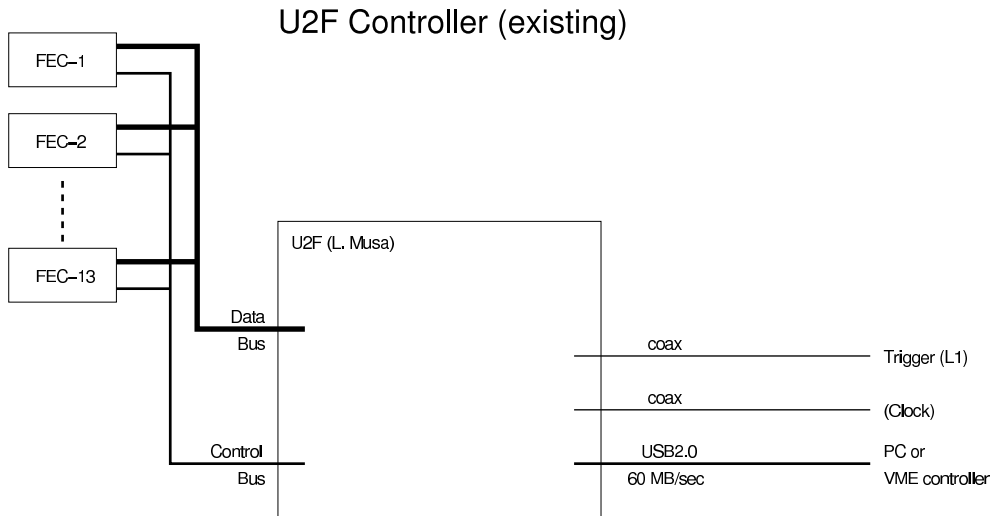


Fig. 28. Current readout hardware for RTPC.

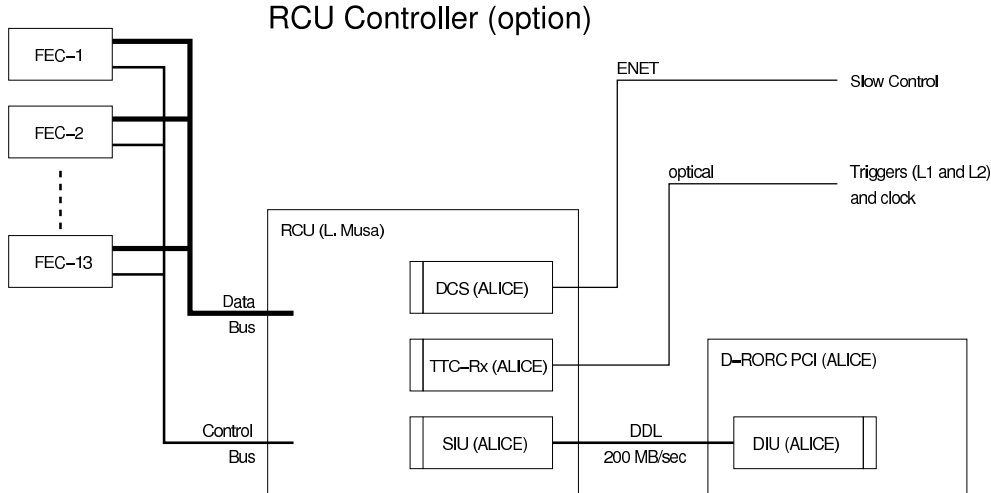


Fig. 29. The proposed readout hardware for RTPC.

detector readout is shown in Fig. 28.

We proposed to change the readout controller hardware to the standard RCU. This hardware consists of the main controller board (RCU), connected via the same buses to the FECs, RCU daughter card for the optical transmission of the data up to 200 MB/s (SIU), RCU daughter card with receiver of optically supplied trigger, RCU daughter card for the slow controls system, and a Readout Receiver Card (RORC) in PCI format with a Destination Interface Unit (DIU). The RORC can be plugged into any PC. This solution would require to purchase at least three RCU cards (two for the two half-cylinders and at least one spare), three SIU daughter cards, three DIU daughter cards, and three RORC PCI cards. The software for the Detector Data Link (DDL) will be provided by the ALICE DAQ group and limited support supplied. Changes to the code have to be done by the user or negotiated with the ALICE DAQ group. The price for the hardware breaks into two components. The ALICE TPC group supplies the RCUs for about 1,000 CHF per link and the ALICE DAQ group supplies the rest for around 1,000 to 2,000 CHF per link (we would need at least three, see above). Depending on the availability of components, ALICE may not be able to supply the hardware, but can help obtaining the boards from the vendors. Group buys with other interested groups are an option. The total price for the hardware will not exceed \$10,000. The optional hardware setup is shown in Fig. 29. This option needs to be integrated into the CLAS DAQ. A new ROC would need to be set up, probably a PC box with two PCI slots running the Linux operating system. This would also require software development to integrate the ALICE DDL software and also to write new code for the ROC. We strongly believe that implementing these modifications will allow us to reach trigger rates 2 kHz .

## References

- [1] J. J. Aubert et al. The ratio of the nucleon structure functions  $F_2^n$  for iron and deuterium. Phys. Lett., B123:275, 1983.
- [2] Donald F. Geesaman, K. Saito, and Anthony William Thomas. The nuclear EMC effect. Ann. Rev. Nucl. Part. Sci., 45:337–390, 1995.
- [3] Abhay Deshpande, Richard Milner, Raju Venugopalan, and Werner Vogelsang. Study of the fundamental structure of matter with an electron ion collider. Ann. Rev. Nucl. Part. Sci., 55:165–228, 2005.
- [4] Michele Arneodo. Nuclear effects in structure functions. Phys. Rept., 240:301–393, 1994.
- [5] Gerald A. Miller and Jason Robert Smith. Return of the EMC effect. Phys. Rev., C65:015211, 2002.
- [6] Anthony William Thomas. New insight into nuclear structure from QCD. Annalen Phys., 13:731–739, 2004.
- [7] Anthony William Thomas, Pierre A. M. Guichon, Derek Bruce Leinweber, and Ross Daniel Young. Towards a connection between nuclear structure and QCD. Prog. Theor. Phys. Suppl., 156:124–136, 2004.
- [8] S. Liuti and S. K. Taneja. Microscopic description of deeply virtual Compton scattering off spin-0 nuclei. Phys. Rev., C72:032201, 2005.
- [9] Amir H. Rezaeian and Hans-Juergen Pirner. The nuclear matter stability in a non-local chiral quark model. Nucl. Phys., A769:35–52, 2006.
- [10] Alexander Selem and Frank Wilczek. Hadron systematics and emergent diquarks. 2006.
- [11] Mark G. Alford, Andreas Schmitt, Krishna Rajagopal, and Thomas Schafer. Color superconductivity in dense quark matter. 2007.
- [12] Zhen-min He, Xiao-xia Yao, Chun-gui Duan, Guang-lie Li, and Hon-gan Peng. Double  $Q^2$ -rescaling model and the nuclear effect of the parton distribution functions. Eur. Phys. J., C4:301–306, 1998.
- [13] Alberto Accardi, D. Grunewald, V. Muccifora, and H. J. Pirner. Atomic mass dependence of hadron production in deep inelastic scattering on nuclei. Nucl. Phys., A761:67–91, 2005.
- [14] A. Kirchner and Dieter Mueller. Deeply virtual Compton scattering off nuclei. Eur. Phys. J., C32:347–375, 2003.
- [15] M. Diehl. Generalized parton distributions. Phys. Rept., 388:41–277, 2003.
- [16] A. V. Belitsky and A. V. Radyushkin. Unraveling hadron structure with generalized parton distributions. Phys. Rept., 418:1–387, 2005.

- [17] Dieter Mueller, D. Robaschik, B. Geyer, F. M. Dittes, and J. Horejsi. Wave functions, evolution equations and evolution kernels from light-ray operators of QCD. Fortschr. Phys., 42:101, 1994.
- [18] Matthias Burkardt. Impact parameter dependent parton distributions and off-forward parton distributions for  $\zeta \rightarrow 0$ . Phys. Rev., D62:071503, 2000.
- [19] M. Diehl. Generalized parton distributions in impact parameter space. Eur. Phys. J., C25:223–232, 2002.
- [20] Andrei V. Belitsky and Dieter Mueller. Nucleon hologram with exclusive lepton production. Nucl. Phys., A711:118–126, 2002.
- [21] Matthias Burkardt. Transverse deformation of parton distributions and transversity decomposition of angular momentum. Phys. Rev., D72:094020, 2005.
- [22] C. Munoz Camacho et al. Scaling tests of the cross section for deeply virtual Compton scattering. Phys. Rev. Lett., 97:262002, 2006.
- [23] F. X. Girod. Deeply Virtual Compton Scattering with CLAS. arXiv:0711.0755 [hep-ex], 2007.
- [24] Xiang-Dong Ji. Gauge invariant decomposition of nucleon spin. Phys. Rev. Lett., 78:610–613, 1997.
- [25] A. V. Radyushkin. Nonforward parton distributions. Phys. Rev., D56:5524–5557, 1997.
- [26] John P. Ralston and Bernard Pire. Femto-photography of protons to nuclei with deeply virtual Compton scattering. Phys. Rev., D66:111501, 2002.
- [27] A. Airapetian et al. Measurement of the beam spin azimuthal asymmetry associated with deeply-virtual Compton scattering. Phys. Rev. Lett., 87:182001, 2001.
- [28] S. Stepanyan et al. First observation of exclusive deeply virtual Compton scattering in polarized electron beam asymmetry measurements. Phys. Rev. Lett., 87:182002, 2001.
- [29] C. Adloff et al. Measurement of deeply virtual Compton scattering at HERA. Phys. Lett., B517:47–58, 2001.
- [30] S. Chekanov et al. Measurement of deeply virtual Compton scattering at HERA. Phys. Lett., B573:46–62, 2003.
- [31] S. Chen et al. Measurement of deeply virtual Compton scattering with a polarized proton target. Phys. Rev. Lett., 97:072002, 2006.
- [32] F. Ellinghaus, R. Shanidze, and J. Volmer. Deeply-virtual Compton scattering on deuterium and neon at HERMES. AIP Conf. Proc., 675:303–307, 2003.
- [33] M. Mazouz et al. Deeply Virtual Compton Scattering off the neutron. Phys. Rev. Lett., 99, 2007.

- [34] V. Guzey and M. Strikman. DVCS on spinless nuclear targets in impulse approximation. Phys. Rev., C68:015204, 2003.
- [35] V. Guzey and M. Siddikov. On the A-dependence of nuclear generalized parton distributions. J. Phys., G32:251–268, 2006.
- [36] Sergio Scopetta. Generalized parton distributions of He-3. Phys. Rev., C70:015205, 2004.
- [37] J. Gomez et al. Measurement of the A-dependence of deep inelastic electron scattering. Phys. Rev., D49:4348–4372, 1994.
- [38] S. Liuti and S. K. Taneja. Nuclear medium modifications of hadrons from generalized parton distributions. Phys. Rev., C72:034902, 2005.
- [39] M. V. Polyakov. Generalized parton distributions and strong forces inside nucleons and nuclei. Phys. Lett., B555:57–62, 2003.
- [40] Davison E. Soper. The Parton Model and the Bethe-Salpeter Wave Function. Phys. Rev., D15:1141, 1977.
- [41] Matthias Burkardt. Impact parameter space interpretation for generalized parton distributions. Int. J. Mod. Phys., A18:173–208, 2003.
- [42] S. Liuti. Generalized parton distributions and transversity in nucleons and nuclei. Nucl. Phys., A755:565–570, 2005.
- [43] Xiang-Dong Ji and Jonathan Osborne. One-loop corrections and all order factorization in deeply virtual Compton scattering. Phys. Rev., D58:094018, 1998.
- [44] John C. Collins and Andreas Freund. Proof of factorization for deeply virtual compton scattering in QCD. Phys. Rev., D59:074009, 1999.
- [45] Andrei V. Belitsky, Dieter Mueller, A. Kirchner, and A. Schafer. Twist-three analysis of photon electroproduction off pion. Phys. Rev., D64:116002, 2001.
- [46] S. Stepanyan, I. Aznaurian, C. Salgado, P. Eugenio, et al. Meson spectroscopy in the Coherent Production on  $^4\text{He}$  with CLAS. JLab Experiment E07-009, 2007.
- [47] V. Burkert, L. Elouadrhiri, M. Garçon, and S. Stepanyan. Deeply Virtual Compton Scattering with CLAS at 6 GeV. JLab Experiment E01-113, 2001.
- [48] H. Fenker, C. Keppel, S Kuhn, W Melnitchouk, et al. JLab Experiment E03-012, 2003.
- [49] R. Niyazov and S. Stepanyan. CLAS-NOTE 2005-021, 2005.
- [50] F.-X. Girod and M. Garçon. CLAS-NOTE 2005-001, 2005.
- [51] F.-X. Girod. CLAS-NOTE 2005-023, 2005.
- [52] F.-X. Girod. Deeply Virtual Compton Scattering (Beam Spin Asymmetries) for the study of Generalized Parton Distributions (PhD Thesis in French), 2006.

- [53] G. R. Goldstein and J. F. Owens.  $\text{Pi}0$  photoproduction in a weak-regge-cut model. Phys. Rev., D7:865–879, 1973.
- [54] G. Goldstein. Private Communication, 2007.
- [55] P. Bertin, C. Hyde-Wright, R. Ransome, F. Sabatié, et al. JLab Experiment E00-110, 2000.
- [56] P. Bertin, C. Hyde-Wright, F. Sabatié, E Voutier, et al. JLab Experiment E03-106, 2003.
- [57] Andrei V. Belitsky, Dieter Mueller, and A. Kirchner. Theory of deeply virtual Compton scattering on the nucleon. Nucl. Phys., B629:323–392, 2002.